Atmospheric
Measurement
Techniques

The CU 2-D-MAX-DOAS instrument – Part 1: Retrieval of 3-D distributions of NO_2 and azimuth-dependent OVOC ratios

I. Ortega[1,2], T. Koenig[1,2], R. Sinreich[1], D. Thomson[2,3], and R. Volkamer[1,2]

[1]Department of Chemistry and Biochemistry, University of Colorado, Boulder, CO, 80309, USA
[2]Cooperative Institute for Research in Environmental Sciences (CIRES), Boulder, CO, 80309, USA
[3]Original Code Consulting, Boulder, CO, 80305, USA

Correspondence to: R. Volkamer (rainer.volkamer@colorado.edu)

Abstract. We present an innovative instrument telescope and describe a retrieval method to probe three-dimensional (3-D) distributions of atmospheric trace gases that are relevant to air pollution and tropospheric chemistry. The University of Colorado (CU) two-dimensional (2-D) multi-axis differential optical absorption spectroscopy (CU 2-D-MAX-DOAS) instrument measures nitrogen dioxide (NO_2), formaldehyde (HCHO), glyoxal (CHOCHO), oxygen dimer (O_2–O_2, or O_4), and water vapor (H_2O); nitrous acid (HONO), bromine monoxide (BrO), and iodine monoxide (IO) are among other gases that can in principle be measured. Information about aerosols is derived through coupling with a radiative transfer model (RTM). The 2-D telescope has three modes of operation: mode 1 measures solar scattered photons from any pair of elevation angle ($-20° <$ EA $< +90°$ or zenith; zero is to the horizon) and azimuth angle ($-180° <$ AA $< +180°$; zero being north); mode 2 measures any set of azimuth angles (AAs) at constant elevation angle (EA) (almucantar scans); and mode 3 tracks the direct solar beam via a separate view port. Vertical profiles of trace gases are measured and used to estimate mixing layer height (MLH). Horizontal distributions are then derived using MLH and parameterization of RTM (Sinreich et al., 2013). NO_2 is evaluated at different wavelengths (350, 450, and 560 nm), exploiting the fact that the effective path length varies systematically with wavelength. The area probed is constrained by O_4 observations at nearby wavelengths and has a diurnal mean effective radius of 7.0 to 25 km around the instrument location; i.e., up to 1960 km^2 can be sampled with high time resolution. The instrument was deployed as part of the Multi-Axis DOAS Comparison campaign for Aerosols and Trace gases (MAD-

CAT) in Mainz, Germany, from 7 June to 6 July 2013. We present first measurements (modes 1 and 2 only) and describe a four-step retrieval to derive (a) boundary layer vertical profiles and MLH of NO_2; (b) near-surface horizontal distributions of NO_2; (c) range-resolved NO_2 horizontal distribution measurements using an "onion-peeling" approach; and (d) the ratios HCHO to NO_2 (R_{FN}), CHOCHO to NO_2 (R_{GN}), and CHOCHO to HCHO (R_{GF}) at 14 pre-set azimuth angles distributed over a 360° view. Three-dimensional distribution measurements with 2-D-MAX-DOAS provide an innovative, regional perspective of trace gases as well as their spatial and temporal concentration gradients, and they maximize information to compare near-surface observations with atmospheric models and satellites.

1 Introduction

Over the past decade the multi-axis differential optical absorption spectroscopy (MAX-DOAS) technique (Hönninger et al., 2004; Wittrock et al., 2004) has been increasingly used to conduct simultaneous measurements of atmospheric trace gas species and their vertical distribution in the lowermost troposphere (Frieß et al., 2006; Roscoe et al., 2010; Irie et al., 2011; Wagner et al., 2011). Species that can be measured include but are not limited to oxides of nitrogen (NO_2) (Wittrock et al., 2004; Sinreich et al., 2005) and the oxygenated volatile organic compounds (OVOCs) formaldehyde (HCHO) (Heckel et al., 2005) and glyoxal (CHO-CHO) (Sinreich et al., 2010). NO_2 plays an important role in the formation of ozone (O_3), which is linked tightly to

air quality by a nonlinear photochemical mechanism involving volatile organic compounds (VOCs) (Finlayson-Pitts and Pitts Jr., 2000). The oxidation of VOC leads also to the formation of OVOCs that form secondary organic aerosol (SOA) (Finlayson-Pitts and Pitts Jr., 2000; Volkamer et al., 2007; Zhang et al., 2007; Jimenez et al., 2009).

MAX-DOAS instruments collect scattered sunlight at different elevation angles (EAs) above the horizon. Spectra recorded at several EAs between the horizon and the zenith view greatly enhanced photon paths and sensitivity inside the boundary layer, which can be used to derive vertical profile information (Hönninger et al., 2004). Traditional MAX-DOAS observations have been performed using one or two azimuth views, and they have highlighted the need for studying inhomogeneities in the air mass close to the instruments (Brinksma et al., 2008). Thus far, the analysis of MAX-DOAS measurements has been limited to at most four azimuth angles (AAs). For example, Wagner et al. (2011) used three telescopes to measure at three fixed azimuth views and several EAs simultaneously to estimate HCHO and NO_2. Recently, Sinreich et al. (2013) introduced a parameterization approach to interpret measurements of near-surface concentrations of NO_2 in three azimuth directions and demonstrated the validity of this approach by comparing with two long-path DOAS instruments facing in opposite directions. Wang et al. (2014) presented measurements under four azimuth viewing angles and with a fixed (low) EA to retrieve surface mixing ratios of several trace gases. Two-dimensional multi-axis differential optical absorption spectroscopy (2-D-MAX-DOAS) is a rapidly emerging technique that points to any AA; the data interpretation is complex. Piters et al. (2012) describes several 2-D-MAX-DOAS instruments from the [Belgian Institute for Space Aeronomy (BIRA), University of Bremen, University of Heidelberg, Washington State University, and NASA. Thus far, only direct sun irradiance measurements with a 2-D telescope have been used to obtain columns of NO_2 without sophisticated radiative transfer calculations (Herman et al., 2009). A retrieval strategy to measure 3-D distributions of gases independent of solar position is complex, and currently missing in the literature to the best of our knowledge. Our retrieval strategy exploits 2-D-MAX-DOAS measurements very efficiently; i.e., a full profile retrieval is conducted for a subset (here one) azimuth direction and used to assess azimuth dependencies of near-surface volume mixing ratio (VMR) using a parameterization approach that builds on Sinreich et al. (2013).

Different inversion strategies have been developed for the quantitative retrieval of trace gases from MAX-DOAS measurements. These inversion algorithms have the goal of converting the primary output of the DOAS analysis, called differential slant column density (dSCD), into comparable information such as vertical concentration profiles, which are not dependent on the measurement geometry or the state of the atmosphere. The retrieval strategies can be divided into (1) full inversion approaches, for instance, optimal estima-

tion (OE) (Rodgers, 1990, 2000) for the retrieval of vertical profiles accomplishing 2–3 degrees of freedom (DOF) (Schofield et al., 2004; Frieß et al., 2006; Irie et al., 2011; Clémer et al., 2010; Hendrick et al., 2014), and (2) parameterization methods which simplify the transfer model and provide fast results with less computational effort (Sinreich et al., 2013; Wagner et al., 2011; and Li et al., 2010).

In this work, the characterization of the University of Colorado (CU) 2-D-MAX-DOAS instrument is described. The capabilities of the CU 2-D-MAX-DOAS include (1) the traditional off axis (EA scan) at any AA, (2) the AA scan at any single EA (almucantar), and (3) direct sun observations. The different modes, defined by software, maximize sampling of the horizontal and vertical distribution of trace gases with a single instrument and with fast time resolution. The aim of this study is to use data from modes 1 and 2 to present an innovative retrieval of 3-D distributions (further development based on Sinreich et al., 2013). Our retrieval of NO_2 combines full inversion and parameterization approaches with "onion peeling". Section 3 introduces the complete retrieval strategy of NO_2 in three dimensions. To our knowledge these are the first attempts by passive remote sensing to retrieve range-resolved horizontal distributions of NO_2 covering 360° around the measurement site. We show that 2-D analysis of trace gas ratios can be used to pinpoint and distinguish VOC emission types (biogenic and/or anthropogenic) and O_3 production hot spots. Finally in Sect. 4 results are presented from a cloud-free case study during the Multi-Axis DOAS Comparison campaign for Aerosols and Trace gases (MAD-CAT). We compare the NO_2 obtained from parameterization approach with OE for one AA, and we compare the spatial scale probed by 2-D-MAX-DOAS at three different wavelengths with that retrieved with the Ozone Monitoring Instrument (OMI) measurements for a test case.

2 Experimental

2.1 The CU 2-D-MAX-DOAS instrument

The CU 2-D-MAX-DOAS instrument is a further development of the one-dimensional CU MAX-DOAS instrument (Coburn et al., 2011). For a detailed characterization of variations of the instrument line shape with wavelength, temperature, integration times, and noise limitations see Coburn et al. (2011). In the following, we present a short description of the CU 2-D-MAX-DOAS system, with emphasis on the 2-D telescope. Briefly, the setup consists of at least two spectrograph/detector units located indoors, a 2-D telescope located outdoors, and an instrument control laptop that is also used for data acquisition and storage. Similar to the one-dimensional device, the complete setup of the CU 2-D-MAX-DOAS was designed to maximize light throughput to facilitate low photon noise in both the UV and visible

spectral ranges (Coburn et al., 2011). This allows the detection of trace gases (e.g., IO, BrO, HCHO, CHOCHO, NO_2, H_2O, and HONO) in addition to the oxygen collision pair O_2–O_2 (O_4). During MAD-CAT (see Sect. 2.2), two Acton SP2150 Imaging Czerny-Turner spectrometers with a highly precise temperature stabilization of 0.005 °C (peak-to-peak variation) were deployed. Each spectrometer was coupled to a Princeton Instrument PIXIS 400 back-illuminated CCD detector. These spectrometer/detector units are identical to the ones described in Baidar et al. (2013); see also Dix et al. (2013) and Oetjen et al. (2013) for the use of the identical spectrometer–detector system during airborne MAX-DOAS applications.

2.1.1 2-D telescope description

A sketch of the 2-D system and the entrance optics of the telescope are shown in Fig. 1. The 2-D telescope allows EA scans (−20 to +90°) at any AA and azimuth scans from −180 to +180° at any EA. The telescope is designed in two tiers. The upper tier contains the optics and a motor (Intelligent Motion Systems Inc. MDrive17) to rotate the housing with the prism for the EA mode, and the lower tier contains a stronger motor (MDrive34) for moving the upper tier to address different AA. There are two view ports, one for the measurement of scattered solar photons, and the other to observe the direct solar beam. The active one can be chosen by opening a shutter just behind the sapphire window. The telescope theoretical field of view (FOV) of the scattered light view port was determined to have an opening angle of 0.95° (full angle). The direct solar light is collected into an integrating sphere with a diameter of 2.54 cm. This sphere serves to homogenize the light, and correct for the possibility of pointing inaccuracies and atmospheric lens effects; this paper does not use any data from the sphere, which will be the subject of a separate publication (Ortega et al., 2015b). The photons are directed onto an f/4 2.54 cm lens via the same optical axis; the lens focuses the light into the mono-fiber, which is coupled to the fiber bundle (see Sect. 2.3). In order to merge the light from both view ports onto a common optical axis, a hole (0.64 cm diameter) was drilled in the prism which is used for the direct sun beam; the scattered light is reflected by 90° along the long side of the prism. The exit port of the integrating sphere is coupled via the hole, and both beams merge past the prism. A custom software package has been developed in LabView to choose between the different scan modes described below.

2.1.2 Telescope capabilities

The capabilities of the CU 2-D-MAX-DOAS instrument include three different modes of measurement: (1) the traditional off-axis (EA) scan at any AA, (2) the AA scan at any EA, and (3) direct sun observations. The different modes of measurement significantly enhance the information that is

accessible about trace gases and aerosol properties that can be retrieved simultaneously. A summary of the three different modes of measurement is shown in Table 1. The particular focus in developing the azimuth scanning capabilities is to enable the measurement of chemical gradients surrounding the measurement site in near-surface air (Part 1 – this work). Part 2 is dedicated to measurements of aerosol microphysical properties in the air column, i.e., effective radius of an aerosol size distribution and complex refractive index.

Pointing accuracy was characterized in some detail, because it plays an important role in the inversion of MAX-DOAS measurements. For example, the exact knowledge of EA is inherent to vertical sensitivity (Hönninger et al., 2004), and the importance of accurate pointing is a prerequisite to ensuring a meaningful comparison/validation of MAX-DOAS instruments (Roscoe et al., 2010). For 2-D systems, knowledge about the pointing further plays an important role for the placement of hot spots, and characterization of horizontal inhomogeneity at any given EA as the AA is varied. The factors that influence knowledge about EA and AA accuracy are mechanical design, angle calibration, and the alignment procedure. In this section we describe the methodology used to ensure maximum accuracy of the telescope pointing.

2.1.3 Alignment procedure

The coordinate system for azimuth viewing is defined as zero corresponding to true north. In order to align the 2-D telescope along the absolute north, we use a three-step process: (1) the raw absolute north is first determined using a digital/manual compass, correcting for the magnetic declination (coarse alignment). (2) We use the scattered solar port and measure the solar radiance distribution at constant EA while varying the AA from left to right of the solar disk. To avoid saturation, the fluxes cannot be measured pointing directly to the sun but need to be performed 5° below and above the sun position. For cloud-free days and angles close to the sun we expect the distribution of radiances to be symmetric with a maximum intensity at the center of the sun's disk. Experimentally, however, a Gaussian fit shows an initial horizontal offset around the sun, which is normally greater than the internal encoder resolution of the AA stepper motor (0.17°). The CU data acquisition software has an option to (3) account for the offset determined from step 2 by software; then we repeat step 2 until the radiances acquired on the left and right side are similar and with an offset smaller than 0.17° (fine alignment). An example of the experimental final alignment is shown in Fig. 2a. In this figure normalized radiances (L, black) are plotted as a function of solar relative azimuth angles (SRAAs). Negative SRAAs represent measurements on the left side (counterclockwise) and positive values are on the right side of the sun (clockwise). A Gaussian fit applied to this example yields the deviation around the center of the sun, which is around 0.06°. The variation of the AA offset over the course of the day is characterized by means

Table 1. The CU 2-D-MAX-DOAS instrument modes of operation.

Mode #	Description	Objective	Temporal and spatial resolution
Mode 1	EA scans of solar scattered photons at any AA angle	Aerosol extinction and trace gas vertical profiles	1–6 min[a] $\sim$ 5–30 km[b]
Mode 2	AA distribution of solar scattered photons at any fixed EA, or solar EA	AA distributions of trace gases, and radiances for aerosol microphysical properties	3–15 min[c] 20 s[c]
Mode 3	Solar direct beam	Raman scattering probability (RSP)	

[a] Acquisition time for a vertical profile; assumption of 6 EA, and acquisition time to retrieve trace gas dSCD of 10–60 s at each EA. [b] Depending on aerosol load and wavelength (see Sect. 4.2). [c] Acquisition time assuming 14 AA, and acquisition time to retrieve trace gas dSCD of 10–60 s, and 1 s for radiances at each AA.
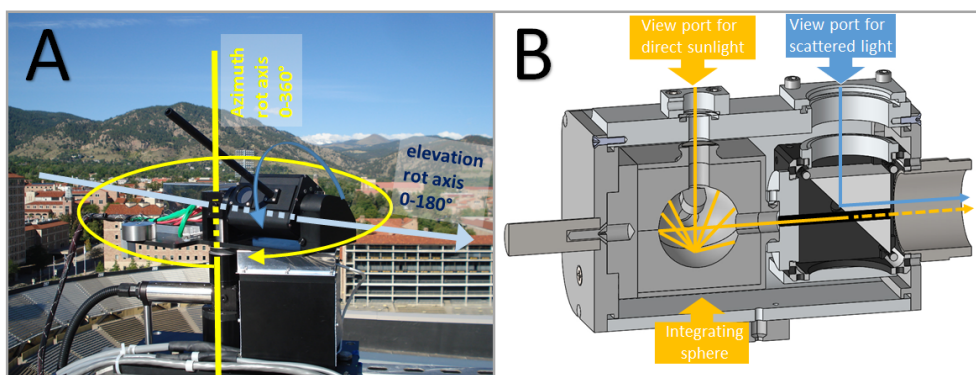

Figure 1. (a) The azimuth and elevation angle scanning (2-D) telescope. The rotation axis for the AA (yellow) and the EA (blue) are marked. **(b)** Sketch of the entrance optics housed by the rotating upper compartment. It contains a through-hole prism to observe scattered photons (blue line) and an integrating sphere to observe direct sunlight (orange line). Two shutters (not shown) are used to block light in one or both ports. A black anodized collimator tube (not shown) is inserted in the prism hole to avoid scattering off the edges of the prism after coming out of the integrating sphere. The lens (not shown) is located on the right side of the prism and integrating sphere. In order to avoid mechanical stress in the optical fiber and allow free mobility of the telescope, the optical fiber is attached in the lowest level of the 2-D telescope and does not move.

of solar aureole measurements (mode 2). In this mode, solar scattered photons at high time resolution (~ 1 s) are collected for SRAAs $> 5°$ typically in steps of 5° up to 180° for the left and right side of the solar disk. Using these measurements a Gaussian function is fitted under homogenous and cloud-free conditions. Figure 2b shows the diurnal average azimuth offset obtained in steps of 5° solar zenith angles (SZAs). The initial alignment of the EA housing is performed using a spirit level. To characterize the absolute EA along the line of sight as viewed by the optics, we measure radiances as a function of EA across a remote object (e.g., the horizon). The gradients across the target are used to determine the EA offset, which is then accounted for by software. Figure 2c shows the normalized radiances measured during the MAD-CAT campaign (see Sect. 2.2), with the 2-D telescope pointing at an AA of 242° towards a hilltop that was chosen as a target because of its well-known geometric EA of 1.1° (J. Remmers, personal communication, 2013). The derivative

of the radiances ($\mathrm{d}L / \mathrm{d}EA$) gives the instantaneous gradients with EAs with a typical Gaussian shape; a Gaussian shaped fit is then applied to the derivative of radiance data to obtain quantitatively the EA offset. The EA offset for the example in Fig. 2c is around 0.35°. We have made no further attempts to account for atmospheric refraction, which for extraterrestrial objects close to the horizon the effect of refraction would be less than 0.2° (depending on temperature, pressure, and wavelength) (Gisi et al., 2011). In order to know the EA offset along different azimuth views, we used a manual digital level. Figure 2d shows the tilt measurements as a function of the AA; here the EA offset is smaller than the resolution of the encoder accuracy of 0.17° for most of the AA.

2.2 The MAD-CAT measurement site

The CU 2-D-MAX-DOAS instrument was deployed as part of the Multi-Axis DOAS Comparison campaign for Aerosols
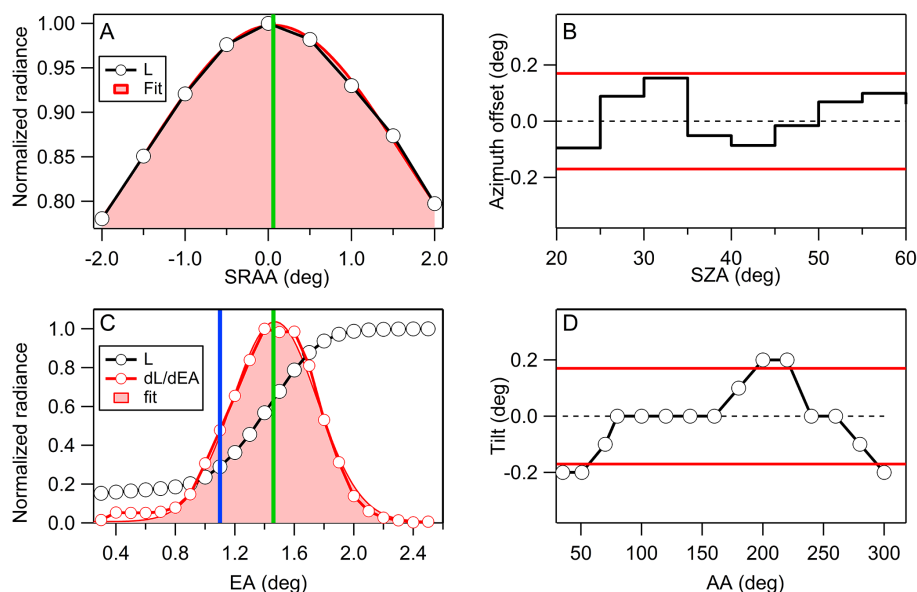
Figure 2. Alignment and characterization of pointing accuracy. **(a)** The AA is adjusted using the moving sun as absolute target. The AA is adjusted until symmetry is found in the aureole flux towards the left and right side of the sun. A Gaussian fit shows the center of the sun is offset by 0.06° (green line). **(b)** The azimuth offset (difference between azimuth of maximum aureole radiance and the absolute solar AA in Euler coordinates) is determined under clear skies as a function of SZA; the accuracy is always better than the resolution of the internal motor encoder (1 encoder step = 0.17°, red lines), and the absolute average is $0.08 \pm 0.04°$. This particular example was performed during the Two-Column Aerosol Project (TCAP, http://campaign.arm.gov/tcap/). **(c)** The EA offset is derived using a remote target (upslope hill) located at the solar azimuth angle of 242°. The black circles are the normalized fluxes, and the red circles are the derivative of the radiances as a function of EA. The theoretical geometric angle of the hill is 1.1° (blue line), and the EA obtained experimentally is 1.46 in this example (green line). **(d)** Tilt measured experimentally using a digital level (red lines; see above).

and Trace gases. MAD-CAT took place in Mainz, Germany, on the roof of the Max Planck Institute for Chemistry (MPIC). The measurement site was located in the western part of the Rhine–Main area surrounded by Frankfurt and several smaller cities. The intensive measurement phase was from 7 June until 6 July 2013, when 11 different MAX-DOAS groups deployed their instruments on the MPIC roof to retrieve trace gas dSCD side by side. The aim of the campaign was to further develop retrieval methods for trace gases and aerosols with and without the presence of clouds and to compare dSCD of trace gases. A description of the MAD-CAT measurement campaign can be found at MPIC, 2013 – http://joseba.mpch-mainz.mpg.de/mad_cat.htm. This work does not discuss comparison results but focuses on the method description and retrievals from a cloud-free case study of 17 June 2013.

2.3 Configuration during MAD-CAT

The wavelength range of one of the spectrometers was set from 329 to 472 nm with a representative optical resolution of 0.78 nm (full width at half maximum, FWHM). The second spectrometer was set to a wavelength range of 432 to 679 nm, covering a large spectral range in the visible, with an optical resolution of 1.65 nm FWHM, which easily allows a retrieval of NO_2 and O_4 at several wavelengths. In

order to know the actual optical resolution and slit function as functions of wavelength, we use a representative Hg or Kr emission line. The 2-D telescope is connected to the spectrometers via an optical cable, which in our case consists of a 15 m × 1.7 mm long optical monofiber that is attached to a 1 m bifurcated fiber bundle consisting of 72 × 145 μm fibers that efficiently distributes the light to the two spectrometer/detector units.

Since an essential part of MAD-CAT was the comparison of results of the different instruments from the MAX-DOAS groups, a specific measurement geometry was determined and applied to all instruments. A "standard" AA of 50.8° with 11 specific EAs was defined as the primary 1-D measurement geometry (see Table 1 and Fig. 1). This azimuth direction enabled an unobstructed view for the smallest EAs. The comparison of the retrieval of trace gases and aerosol properties for all instruments deployed during MAD-CAT had special interest in the EA scan sequence, which has been performed in previous intercomparison campaigns (Roscoe et al., 2010; Pinardi et al., 2013). For the instruments with 2-D capabilities, every 2 h an AA sequence scan was also recommended. In order to investigate the horizontal distribution of trace gases, we continuously measured the EA sequence at the standard AA immediately followed by the AA sequence scan with 14 angles covering the 360° around

Table 2. Configuration of the instrument during the MAD-CAT setup.

Mode	EA (degree)	AA (degree)	Integration time (cycle time resolution)
1	90, 45, 30, 10, 8, 6, 5, 4, 3, 2, 1, 90	50.8	30s[a] ($\sim$ 6min[b])
2	2	5, 37.5, 45, 50.8, 75, 94, 130, 145, 185, 200, 227, 242, 281, 321	30 s[a] ($\sim$ 7 min[b])

[a] Single measurement. [b] Overall time delay to complete the cycle.

the measurement site, which resulted in a higher time resolution (see Table 2). The increase in time resolution could be achieved by the low photon shot noise spectrometer–detector system and a fast telescope response, so that the integration time of each acquired spectrum was set to 30 s. Considering the time for the motors movement, the EA scan sequence took 6 min, while an AA scan sequence took about 7 min to complete; the resulting full measurement cycle was repeated every 13–14 min.

3 DOAS analysis and retrieval strategy

3.1 DOAS analysis of NO₂, HCHO, CHOCHO, and O₄

The spectra collected at different AAs and EAs were analyzed using the DOAS approach as implemented in the Win-DOAS software package (Fayt and Van Roozendael, 2001). The DOAS method uses the specific narrow-band absorption of trace gases (< 5 nm) in the ultraviolet–visible light spectrum and separates them from broadband molecule and aerosol extinction quantifying the trace gases by applying Lambert–Beer law (Platt and Stutz, 2008). The list of trace gas cross sections used in the analysis of NO_2, O_4, HCHO, and CHOCHO is given in Table 3, and the summary of the DOAS analysis settings is listed in Table 4. Most of the absorption cross sections used here are the same as those implemented in previous field campaigns (Roscoe et al., 2010; Pinardi et al., 2013); however we have employed the H_2O cross section from the HITEMP database, which combines the HITRAN 2010 database with theoretical calculations (Rothman et al., 2010). Also, we used the O_4 cross section described in the recent work of Thalman and Volkamer (2013). The zenith spectrum measured at the beginning of mode 1 is used as a reference spectrum in the analysis

Table 3. List of trace gas references used for the DOAS analysis.

No.	Molecule	Reference
1	NO_2 (220 K)	Vandaele et al. (1998)
2	NO_2 (294 K)	Vandaele et al. (1998)
3	O_3 (223 K)	Bogumil et al. (2003)
4	O_3 (243 K)	Bogumil et al. (2003)
5	O_4 (293 K)	Thalman and Volkamer (2013)
6	CHOCHO (298 K)	Volkamer et al. (2005)
7	HCHO (297 K)	Meller and Moortgat (2000)
8	H_2O (296 K)	Rothman et al. (2010)
9	BrO	Fleischmann et al. (2004)
10	Ring	Chance and Spurr (1997)

of all trace gases in mode 1. At the end of mode 1 another zenith spectrum is measured and used to analyze trace gases in mode 2. Thereby we minimize stratospheric contributions and possible variation of stratospheric contribution during a complete cycle. In addition a Ring cross section is calculated from each reference spectrum and included in the fit to account for the "filling in" of Fraunhofer lines due to rotational Raman scattering (Grainger and Ring, 1962; Wagner et al., 2009). The primary product of the DOAS analysis is dSCD as the measured spectra are analyzed with respect to a reference spectrum.

NO_2 and O_4 are retrieved at three different wavelengths (see Table 3) in order to probe different spatial ranges with the optical path length wavelength dependence. We followed the settings given in Roscoe et al. (2010) for the analysis of NO_2 and O_4 in the range of 338–490 nm; however we used the 445–490 nm window range instead of 425–490 nm recommended in Roscoe et al. (2010) since neither of our spectrometers described in Sect. 2.3 do completely cover the wider range. Additionally we evaluated NO_2 in the range of 540–588 nm combined with the O_4 strong band at 577 nm. The analysis of HCHO and CHOCHO was carried out with the higher-resolution spectrometer. The fitting window for HCHO (336.5–359 nm) and most of the settings presented in Table 3 were adapted from the recent HCHO dSCD intercomparison study described in Pinardi et al. (2013). Sensitivity studies of the spectral window chosen for the fit of HCHO were performed (see Fig. S1 in the Supplement) and confirm that this spectral window is stable for different polynomial degrees, and for minimizing the residual and cross correlation with BrO. The fitting window of 434–460 nm was used in order to analyze glyoxal. Similar analysis settings have been used in the past (Sinreich et al., 2010). This interval includes the dual strong absorption of glyoxal at 440 and 454 nm. Further analysis of the glyoxal DOAS settings and extensive results of the glyoxal intercomparison with multiple instruments are planned among other trace gases. Figure 3 shows spectral proof examples of all the windows that were analyzed and used in this work.

Table 4. Summary of the DOAS fitting analysis.

Target	Spectrometer resolution (nm)	Fitting window (nm)	Cross section fitted	Polynomial order
HCHO, NO_2	0.78	336.5–359	1, 2, 3, 4, 5, 7, 9, 10	3
CHOCHO, NO_2	0.78	434–460	1, 2, 3, 5, 6, 8, 10	5
O_4, NO_2	0.78	338–370	1, 2, 3, 4, 5, 7, 9, 10	5
O_4, NO_2	1.65	445–490	1, 2, 3, 5, 6, 8, 10	5
O_4, NO_2	1.65	540–588	1, 2, 3, 5, 8, 10	3

3.2 Retrieval strategy

The objective of obtaining range-resolved NO_2 horizontal distribution measurements is based on an onion-peeling approach of NO_2 measured at multiple wavelengths; it consists of four main steps: (1) aerosol extinction profiles are retrieved at multiple wavelengths by means of a nonlinear inversion method (we employ the approach as described in Prados-Roman et al. (2011) for aircraft MAX-DOAS); (2) multiple wavelength retrieval of NO_2 boundary layer vertical profiles using a linear OE scheme (Rodgers, 2000) and estimation of the mixing layer height (MLH); (3) 360° multiple wavelength azimuth horizontal near-surface average box mixing ratios using the parameterization approach introduced by Sinreich et al. (2013); and (4) applying an onion-peeling approach, making use of different viewing ranges (distance from the site) at different wavelengths to obtain NO_2 as a function of distance from the measurement site. To probe the different spatial scales we apply the steps above for three wavelengths (350, 450, and 560 nm). A detailed sketch of the inversion scheme is illustrated in Fig. 4 and explained briefly in the next sections.

3.2.1 Aerosol extinction vertical profile inversion

The retrieval of multi-wavelength aerosol extinction profiles is based on normalized radiances at a given wavelength, similar to the inversion described in Prados-Roman et al. (2011) for aircraft MAX-DOAS measurements. The idea behind the sun-normalized radiances retrieval builds on the minimization of the cost function in Eq. (1) via the nonlinear Levenberg–Marquardt approach.

$$\left\| \boldsymbol{y}_L - F_L\left(\boldsymbol{x}_L, \boldsymbol{b}\right) \right\|^2_{\mathbf{S}_e^{-1}} \tag{1}$$

In this equation, $\boldsymbol{y}_L$ are the measured sun-normalized radiances $\boldsymbol{y}_L = \ln\left(\frac{L_i(\lambda)}{L_{\text{ref}}(\lambda)}\right)$, $F_L(\boldsymbol{x}, \boldsymbol{b})$ is the sun-normalized radiance simulated with the input parameters $\boldsymbol{b}$ and the aerosol profile $\boldsymbol{x}_L$, and $\mathbf{S}_e$ is the diagonal covariance measurement error matrix. The full spherical Monte Carlo Radiative Transfer Model (McArtim) has been used for this work. It has been shown in Deutschmann et al. (2011) that McArtim is a suitable algorithm to represent the atmospheric radiative transfer in the UV–Vis–IR wavelength range. The pressure and temperature profiles were taken from the US Standard Atmo-

sphere, and the retrieval grid was chosen to be 300 m thick between 0 and 3.3 km to represent the boundary layer. Typical aerosol optical parameters for urban atmosphere were used in the RTM (Dubovik et al., 2002). Assumptions for all the input parameters $\boldsymbol{b}$ (absorption cross section, aerosol optical properties, atmospheric conditions, etc.) used in the forward model are considered in the error propagation.

The wavelengths chosen to calculate the aerosol extinction profiles are 350, 450, and 560 nm, which are representative for the window intervals where NO_2 is retrieved (see Table 3). These wavelengths prevent significant interferences from strong absorbers such as H_2O and O_3. The normalized radiances are calculated with the 90° EA as the reference angle in order to use lower EAs and maximize the information in the boundary layer. The aerosol extinction convergence criteria are achieved when the residuals of the cost function in Eq. (1) fall into a valley under a certain feasible set of extinction profiles calculated with the constrain parameters.

### 3.2.2 NO_2 vertical profile retrieval

Once the aerosol extinction profiles have been derived, they are used to constrain the linear inversion of NO_2 vertical profiles using the EA scan at standard AA. A set of NO_2 dSCDs from the EA scan are related to the trace gas vertical profile $\boldsymbol{x}$ in the following equation:

$$\boldsymbol{y}_{\text{tg}} = \mathbf{K}\boldsymbol{x} + \boldsymbol{\varepsilon}, \tag{2}$$

where $\mathbf{K}$ is the weighting function matrix that expresses the sensitivity of measurement $\boldsymbol{y}_{\text{tg}}$ to the true profile $\boldsymbol{x}$, and $\boldsymbol{\varepsilon}$ represents the measurement and radiative transfer errors. The maximum a posteriori solution to the above problem using OE is given by

$$\boldsymbol{x} = \boldsymbol{x}_a + \left(\mathbf{K}^T \mathbf{S}_\varepsilon^{-1} \mathbf{K} + \mathbf{S}_a\right)^{-1} \mathbf{K}^T \mathbf{S}_\varepsilon^{-1} \left(\boldsymbol{y}_{\text{tg}} - \mathbf{K}\boldsymbol{x}_a\right), \tag{3}$$

where $\boldsymbol{x}_a$ is the a priori profile used to constrain the ill-posed inversion problem (Rodgers, 2000), and $\mathbf{S}_\varepsilon$ and $\mathbf{S}_a$ are the measurement error and a priori error covariance matrices, respectively. $\mathbf{S}_\varepsilon$ is built using the square of the DOAS fit error as the diagonal elements, and the non-diagonal elements were set to 0 assuming the errors are uncorrelated. As an a priori profile we use an exponentially decreasing NO_2 profile with a fixed scale height of 0.5 km and
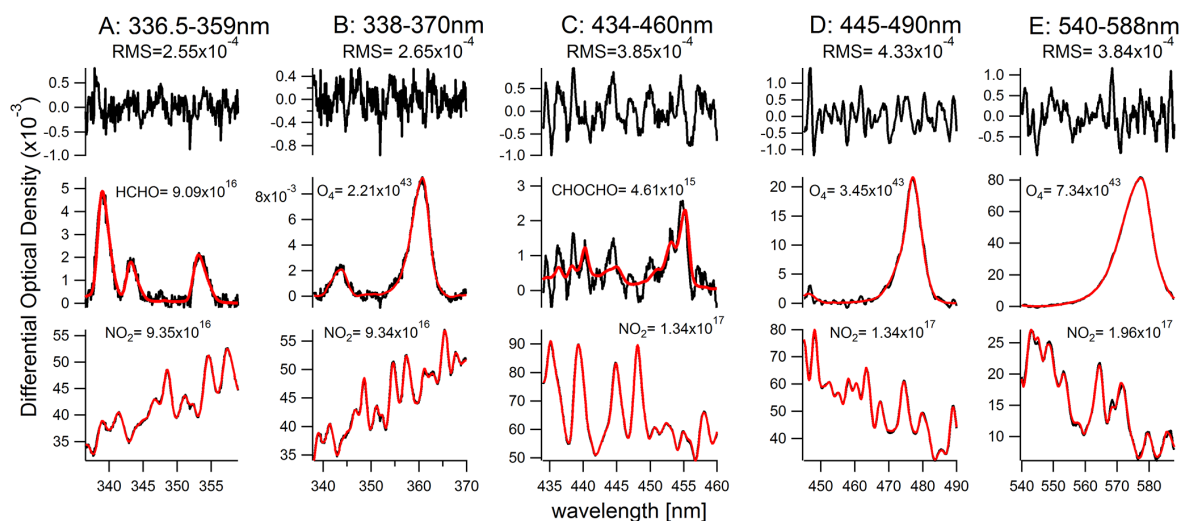
Figure 3. Spectral proofs for the detection of **(a)** HCHO, **(b)** O_4 at 360 nm, **(c)** CHOCHO, **(d)** O_4 at 477 nm, **(e)** O_4 at 577 nm, and NO_2 (all panels) on 17 June 2013 at 14:23 UTC, with $SZA = 43.2°$, $EA = 2°$, and $AA = 50.8°$ from the roof of Max Planck Institute in Mainz, Germany. Black lines represent measured spectra; red lines are scaled reference cross sections in dSCD units for CHOCHO, HCHO, NO_2 (molecules cm^{-2}), and O_4 (molecules^2 cm^{-5}).
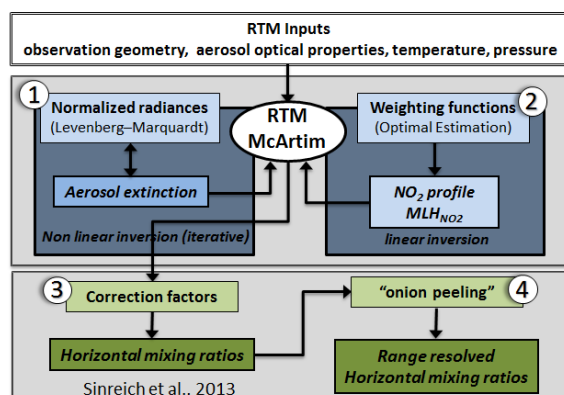
Figure 4. A four-step retrieval is applied: (1) aerosol extinction is determined at O_4 wavelengths by means of nonlinear inversion using normalized radiances; (2) the trace gas vertical profiles are derived (see text). The center shaded area represents the inversion of the EA scan measurements using OE, from which the MLH is determined. The lower shaded area represents parameterization of RTM that uses MLH as input to determine (3) near-surface VMR (Sinreich et al., 2013), and (4) range-resolved NO_2 VMRs using an "onion-peeling" approach and NO_2 measurements at different wavelengths.

5×10^{15} molecules cm^{-2} vertical column density (VCD) at the ground, similar to the approach used in Hendrick et al. (2014). The S_a matrix was treated as a tuned parameter in order to avoid non-real oscillations in the retrieved profiles (Clémer et al., 2010; Baidar et al., 2013; Hendrick et al., 2014). The diagonal elements of the S_a matrix were set to account for large variations, up to 100 %, of the initial a priori profiles. The non-diagonal elements of the S_a matrix

were correlated through the altitudes (z) with an exponential Gaussian decay function (Barret et al., 2003; Clémer et al., 2010):

$$S_a = \sqrt{S_a(i,i) S_a(j,j) \exp\left[-\ln(2)\left(\frac{z_i - z_j}{\gamma}\right)^2\right]}. \quad (4)$$

In this equation z_i and z_j are the altitudes of the ith and jth grid layers, respectively, and γ is the correlation parameter, which was set to 0.3 km, similar to the inversion grid height. The wavelengths used to retrieve NO_2 vertical profiles are the same as for the aerosol extinction profiles (350, 450, and 560 nm).

3.2.3 NO_2 near-surface horizontal distribution

We apply the parameterization approach introduced in Sinreich et al. (2013) to the AA scan to obtain the horizontal near-surface mixing ratios of NO_2. In short, Sinreich et al. (2013) pointed out that dSCD obtained from MAX-DOAS in a single and low EA can be converted into near-surface box average mixing ratios by means of parameterization of the RTM. In the following, we use terminology consistent with that of Sinreich et al. (2013); however we refer to MLH instead of planetary boundary layer (PBL) to avoid confusion with the meteorological term. Briefly, the differential light path of the EA with respect to the reference is determined by means of O_4 dSCD weighted by a correction factor. The correction factor, f_c, accounts for the different O_4 and NO_2 vertical profile shapes and the difference in absorption wavelengths. Sinreich et al. (2013) showed that this method does not depend on the actual aerosol load and that it only weakly depends on

the aerosol layer height, if sufficient aerosol is present. This was assessed in Sinreich et al. (2013) by a "collapsing" of the O_4 dSCDs in a set of two low EAs, which is however not a prerequisite for this approach to work for very low EAs (see Supplement text in Sinreich et al., 2013; Wang et al., 2014). An important prerequisite for calculating f_c is knowledge about the trace gas MLH. As long as this height is higher than 500 m, the method is insensitive to the actual value of the trace gas layer height. We apply this method to multiple wavelengths to average NO_2 over different horizontal distances. At each wavelength the near-surface volume mixing ratio of NO_2 can be evaluated using the following equation (Sinreich et al., 2013):

$$VMR_{NO_2} = \frac{1}{f_c} \frac{dSCD_{NO_2} \cdot C_{O_4}}{dSCD_{O_4}} \frac{1}{CF}, \tag{5}$$

where $dSCD_{NO_2}$ and $dSCD_{O_4}$ are the measured dSCD for NO_2 in units of $molec \times cm^{-2}$ and O_4 in units of $molec^2 \times cm^{-5}$, respectively; CF is the conversion factor from the concentration to the VMR; C_{O_4} the concentration of O_4 in units of $molec \times cm^{-3}$; and f_c (unitless) the correction factor which adjusts for the differences in the NO_2 and the O_4 profile shapes. The correction factor is calculated by the following equation:

$$f_c = \frac{dAMF_{NO_2} \cdot MLH_{NO_2} \cdot C_{O_4}}{dAMF_{O_4} \cdot VCD_{O_4}}, \tag{6}$$

where $dAMF_{NO_2}$ and $dAMF_{O_4}$ (unitless) are the differential air mass factors (AMF) for NO_2 and O_4, respectively; VCD_{O_4} is a typical O_4 VCD in units of $molec^2 \times cm^{-5}$; and MLH_{NO_2} is the NO_2 MLH in units of centimeters. The MLH_{NO_2} represents the depth of the lower atmosphere where NO_2 is dispersed as a result of turbulent vertical mixing processes. In a first step, the MLH_{NO_2} is estimated using the NO_2 vertical profiles (see Sect. 4.1.2), and it is used subsequently to calculate the value of f_c. The dAMF is defined as the difference in AMF (light path enhancement in the atmosphere relative to vertical path through the atmosphere) between the measured and reference viewing geometry. Generally, dAMFs are calculated with a RTM at low uncertainty; however the calculation of dAMFs depends on the state of the atmosphere (aerosol load), geometry of the measurements, and wavelength (Wagner et al., 2007). Although the correction factors and the sensitivity were presented in Sinreich et al. (2013), and applied in Wang et al. (2014), these studies explored a limited subset of geometries and wavelength ranges. In this work we expand significantly the number of AAs and wavelength ranges. This requires a more detailed description of the correction factors and their dependency on input parameters to the RTM. In order to know the variability of the correction factors, we change the magnitude of different input parameters such as the aerosol asymmetry parameter (g), single scattering albedo (SSA), surface albedo (SA), and NO_2 as well as aerosol load and vertical extent. Table 5 shows the main input parameters to calculate f_c and its

variability for the three wavelengths. A good starting point for the aerosol optical properties is using the aerosol column properties derived from the co-located AErosol RObotic NETwork (AERONET) sun photometer as shown in Table 5. Barnard et al. (2008) showed that the SSA at UV wavelengths can be significantly lower than in the visible due to light absorption by "brown-carbon" aerosols. The discrete wavelengths used by AERONET do not cover 350 nm; hence we use a lower limit of SSA to calculate the variability in the UV (Table 5). The RTM is parameterized by using the aerosol load determined in Sect. 4.1.1. In contrast, the diurnal geometry of the measurements, i.e., the SZA and SRAA, are known parameters. The magnitude of f_c and its variability are shown in Sect. 4.2.

3.3 Range-resolved NO_2: "onion peeling"

The differential effective path length (L_{eff}), defined as the path length from the effective scattering event to the telescope corrected by the difference in the O_4 and NO_2 profiles shapes in the boundary layer, is calculated with the equation

$$L_{eff} = \frac{dSCD_{O_4}}{C_{O_4}} f_c. \tag{7}$$

Similarly, the vertical extent of the box-profile average VMR is represented by the effective height (H_{eff}) calculated as $H_{eff} = L_{eff} \cdot \sin(EA)$. In order to obtain range-resolved NO_2 mixing ratios we exploit the fact that L_{eff} and sensitivity depend on the atmospheric and scattering conditions. The strong positive wavelength dependence of scattering means that the shorter the wavelength the shorter the path length. The onion-peeling approach is applied for the azimuth scan in order to derive NO_2 mixing ratios related to different air masses along the same azimuth viewing angle. A graphical representation of the onion-peeling method is shown in Fig. 5. The azimuth scan is divided into different horizontal layers determined by the differential effective path length at each wavelength. The radii of the blue, green, and red circles represent the path length realized at 350 ($L_{eff,350}$), 450 ($L_{eff,450}$), and 560 nm ($L_{eff,560}$) over the full azimuth scan, respectively. The onion peeling defines three different rings, or layers, L_1, L_2, and L_3; the objective is to obtain the respective average volume mixing ratios VMR_1, VMR_2, and VMR_3 within each of these layers. L_1 is directly identified as the retrieval at 360 nm. L_2 and L_3 are determined as the differences between 450 and 360 nm ($L_{eff,450} - L_{eff,360}$) and between 560 and 450 nm ($L_{eff,560} - L_{eff,450}$), respectively. The average mixing ratios are calculated using the following equation:

$$VMR_2 = \frac{\left[VMR_{450} \cdot L_{eff,450} - VMR_{360} \cdot L_{eff,360}\right]}{L_2}, \quad (8)$$

$$VMR_3 = \frac{\left[VMR_{560} \cdot L_{eff,560} - VMR_{450} \cdot L_{eff,450}\right]}{L_3},$$

where VMR_2 and VMR_3 represent the differences in VMR in each circle weighted by the differential effective path length in L_2 and L_3, respectively.

3.4 Azimuth trace gas ratios: metric for anthropogenic/biogenic influence and O_3 formation

Prior studies have illustrated the use of the HCHO-to-NO$_2$ (R_{FN}) ratio as a metric to understand O_3 production (Duncan et al., 2010) and VOC emission types by means of the CHOCHO-to-HCHO ratio (R_{GF}, Vrekoussis et al., 2010; Di-Gangi et al., 2012). The application of the ratios to the azimuth scan enables the identification of hot spots and inhomogeneities around the instrument location. Additionally the CHOCHO-to-NO$_2$ ratio (R_{GN}) was calculated. The azimuthal distribution of the trace gas ratios in the boundary layer directly uses the respective trace gas dSCDs. R_{FN} and R_{GN} are calculated with the dSCD obtained in the same wavelength window to assure the optical path lengths are directly comparable. However, R_{GF} needs special attention since HCHO and CHOCHO retrievals employ different wavelengths during the DOAS analysis (Table 3) and thus reflect different optical paths. In order to account for the different spatial scales probed at UV and visible wavelengths, we use the O_4 dSCD measured at wavelengths that closely resemble those of the OVOCs to derive a correction factor. The R_{GF} used in this work is calculated by applying the following equation:

$$R_{GF} = \left(\frac{CHOCHO_{dSCD}}{HCHO_{dSCD}}\right) \cdot R_{O_4}, \quad (9)$$

where R_{O_4} is equal to the O_4 dSCD ratio in the UV divided by those of the visible. Another important advantage which arises from using dSCD in the azimuth scan is that no complex and laborious RTM is necessary, resulting in a fast retrieval to determine near-real-time air mass chemistry.

4 Results and discussions

4.1 Boundary layer vertical profiles

4.1.1 Aerosol extinction: comparison of AOD with AERONET

Figure 6 shows the multi-wavelength aerosol extinction diurnal vertical distribution using the standard AA of 50.8°. The aerosol extinction follows the typical wavelength dependence, where it increases as the wavelength decreases. The
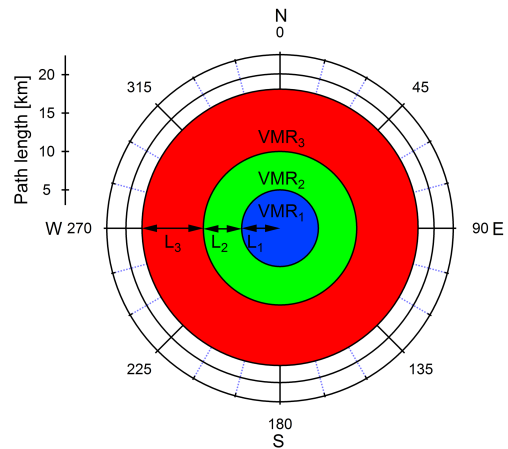
Figure 5. Conceptual sketch of the onion-peeling approach. See text for details.

integrated extinction profiles over altitude, known as aerosol optical depth (AOD), are compared with the AOD retrieved with the co-located AERONET sensor to partially demonstrate aerosol homogeneity around the site. The AERONET sun photometer uses discrete fixed wavelengths, which are not the same as the wavelengths we applied here; hence the aerosol wavelength dependence (Ångström exponent) is used to interpolate the AOD at the wavelengths of interest. Even though the directionality of AERONET (a solar tracker) and the standard EA scan of the 2-D-MAX-DOAS measurements are different, they show a generally good multi-wavelength AOD agreement with a slope ranging from 0.77 to 0.93 (± 0.03) from the visible to the UV. The agreement between the two instruments could be coincidental, or indicate that the aerosol load around the city of Mainz is homogeneous. Furthermore, observations of the 2-D analysis of O_4 dSCD (elevation angle of 2°) do not show a significant difference with respect to aerosol azimuth distribution.
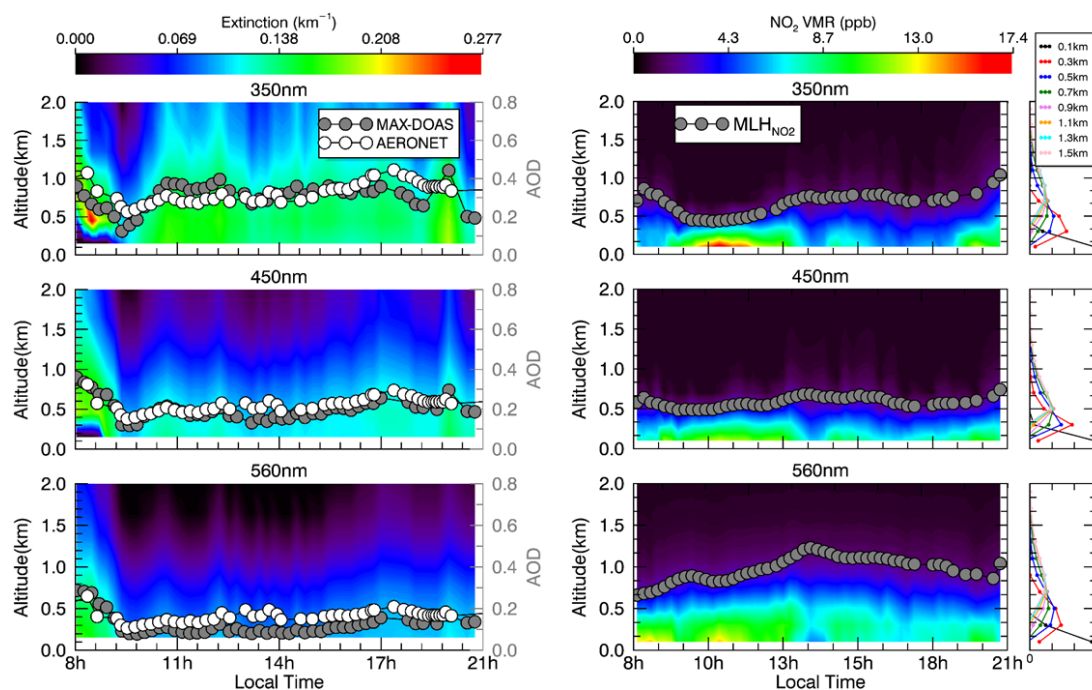
4.1.2 NO$_2$ vertical profile

The diurnal variation of NO$_2$ in the boundary layer is shown in Fig. 6 and indicates an increase of NO$_2$ in the early morning followed by a decrease in the evening. The vertical extent of NO$_2$ in the boundary layer for the three wavelengths is very similar: most of the NO$_2$ is located in the layer below 1 km. Small differences in the NO$_2$ vertical distribution are found for the three wavelengths, and these may be related to the smoothing in the retrieval and to some extent the sensitivity range for each wavelength.

A critical parameter for the calculation of f_c in Eq. (6) is prior knowledge of the MLH (Sinreich et al., 2013). In this work we estimate the MLH using NO$_2$ as a tracer for the vertical extent of mixing. In general, the estimation of the altitude sensitivity in the vertical profile retrieval is well represented by the averaging kernels and eigenvectors which are derived in OE (Rodgers 2000; Frieß et al., 2006). Ac-

Table 5. Sensitivity studies for the correction factor.

Parameter	360 nm	450 nm	560 nm
MLH (km)	Uncertainty derived from OE		
Asymmetry parameter (g)	0.73	0.7	0.67
	0.7 (AERONET)	0.67 (AERONET)	0.64 (AERONET)
	0.67	0.64	0.61
SSA	0.78	0.94 (AERONET)	0.93 (AERONET)
	0.95 (AERONET)	0.97	0.96
	0.98		
SA	0.04	0.05	0.06
	0.06	0.07	0.08

Figure 6. Diurnal aerosol extinction (left) and NO_2 vertical profiles (right) at three different wavelengths (from top to bottom: 350, 450, and 560 nm) on Monday, 17 June 2013, above the MAD-CAT site for the standard AA of 50.8°. The AOD determined by MAX-DOAS at the O_4 wavelengths is compared with the AOD interpolated from co-located AERONET measurements which uses a different geometry (AOD towards the direction of the solar beam). The MLH_{NO_2} is estimated as the $1/(2e)$ decrease of the near-surface NO_2 VMR at each wavelength. An averaging kernel example around midday is shown on the right plot of each NO_2 diurnal profile plot. The DOF for each case are ~ 2.0.

cording to the averaging kernel of the NO_2 vertical profile the boundary layer is well constrained by the measurements (see Fig. 6). The number of DOF is 2–2.5 for each wavelength, with the highest sensitivity close to the surface (0–200 m layer). NO_2 is a good tracer for MLH, because it has a relatively short effective lifetime (limited to few hours by $OH + NO_2$ reactions). The MLH can be described as the depth of the lower atmosphere in which the NO_2, emitted mostly as NO and formed within this layer, is dispersed almost uniformly as a result of turbulent vertical mixing processes (Emeis and Schäfer, 2006). Usually NO_2 decreases strongly above this mixing height as chemical re-

actions remove NO_2 as a result of photochemistry and hydrolysis of N_2O_5 at the surface of wet aerosols (Baidar et al., 2013; Ryerson et al., 2013). In this work we approximate the MLH_{NO_2} as the altitude over which the NO_2 mixing ratio decreases to $1/(2e)$ of the near-surface value. The gray circles in the NO_2 vertical distribution plot of Fig. 6 represent the MLH_{NO_2} determined by this definition. As can be seen, the MLH_{NO_2} varies as a function of the time of day. There is some sensitivity to a residual layer in the early morning. Around 10:00 local time (LT) the MLH_{NO_2} starts to increase due to the development of the convective boundary layer and efficient mixing. The MLH_{NO_2} variation for the

different wavelengths may be caused by the smoothing factor in the NO$_2$ vertical profile retrieval, though a mountain terrain effect may also play a role at the longer wavelengths. For the calculation of f_c the time-resolved average MLH$_{NO_2}$ obtained with the three wavelengths is used and the standard deviation is used to estimate its variability. The sensitivity of the height distribution of NO$_2$ on f_c was tested with an independent method. This approach assumes a NO$_x$ box profile shape, assigns the near-surface NO$_2$ VMR from OE, and assigns an effective mixing height (MLH$_{NO_2,eff}$) based on the measured NO$_2$ VCD. The retrieved MLH$_{NO_2,eff}$ was compared with the MLH$_{NO_2}$ calculated before. We found a good correlation ($R^2 = 0.81$) with a linear fit of MLH$_{NO_2,eff} = 0.93 \pm 0.06 \cdot$ MLH$_{NO_2} + 0.10 \pm 0.04$ [$R^2 = 0.81$]. The resulting MLH$_{NO_2,eff}$ is within the error near the lower limit of the standard deviation, which is used to calculate the variability associated with the MLH$_{NO_2}$ as mentioned before.

4.2 Azimuth distribution of NO$_2$ VMR

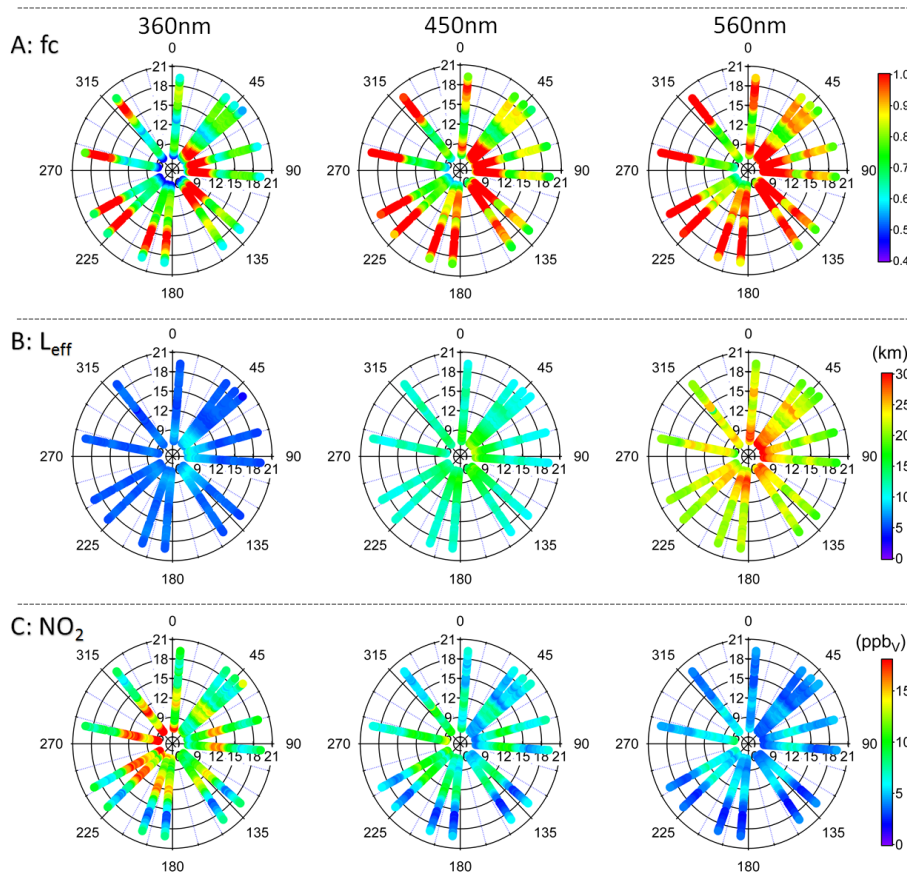### 4.2.1 Correction factors and effective path length

The results of the azimuthal diurnal variation of the correction factors are shown in the form of a polar plot in Fig. 7a. The radii of the polar plots shown in this section represent the local time and the color code the magnitude of the parameters. The values of f_c represent the mean values of the sensitivity studies shown in Sect. 3.2.3 and summarized in Table 5. A value of $f_c = 1.00$ means that the radiation field is equally sensitive to NO$_2$ and O$_4$; a value of $f_c < 1$ means that the sensitivity increases towards detecting O$_4$ with respect to NO$_2$. A detailed description of the variability and geometry dependency is given in Sinreich et al. (2013) and shown in Fig. S2. In short, f_c does not change drastically with the variability of g, SSA, and SA (Sinreich et al., 2013). In contrast, the MLH can have a larger impact. We estimate the variability of f_c to be on the order of 5–8 %. This low error is possible since we estimate the MLH and its variation using NO$_2$ vertical profiles. The most surprising effect is the clear SRAA dependence where f_c increases for SRAA close to the sun, especially for SZA between 40 and 60° (Fig. S2). This behavior is due to low-O$_4$ dAMFs obtained with the RTM. For these cases f_c can in fact exceed unity; however the O$_4$ dSCDs do not show a significant SRAA dependence. This behavior in calculated O$_4$ dAMFs is currently not understood. However, we note that it is consistent with earlier observations that measured O$_4$ dSCD under certain conditions can exceed those calculated by RTM (Clémer et al., 2010; Wagner et al., 2011; Irie et al., 2011, Merlaud et al., 2011). Recent testing of measured O$_4$ dSCD from aircraft found agreement within 2–3 % with those from other geometries (Spinei et al., 2015). For lack of a physical explanation, for the cases when $f_c > 1$ we set f_c to be unity.

Figure 7b shows the diurnal variation of L_{eff} calculated with Eq. (7). The results indicate a strong wavelength de-

pendence, which is exploited in the onion-peeling approach introduced in Sect. 4.3. The 350 nm L_{eff} displays values between 5 and 10 km; the 450 nm one can reach horizontal distances of 10–20 km; and the 560 nm one shows sensitivity to horizontal distances of 18–30 km. In the early morning the L_{eff} is larger, likely due to low-O$_4$ dAMF, and is more evident for the east view due to the low SRAAs. In general, there is not a significant AA dependence, indicating azimuth homogeneity as stated in Sect. 4.1.1.

The diurnal variation of near-surface mixing ratios of NO$_2$ is presented in Fig. 7c. The azimuth inhomogeneity is apparent from this figure, wherein most of the NO$_2$ is located in the west, especially in the early morning ($\sim$ 07:00–08:00) and when the traffic increases and NO$_2$ accumulates ($\sim$ 09:00–11:00). This is surprising, considering that the industrial complex and cities close to the site are located north and northeast, and may indicate that mobile sources continue to be significant contributors to ambient NO$_x$ during morning rush hour. The wind direction and speed can provide further information about transport of the air masses. The daytime values, provided by the MAD-CAT team (https://www.blogs.uni-mainz.de/fb08-ipa/wetter/), are shown in Fig. 8. The main wind direction is northeast with typical wind speed around 2–4 m s^{-1}, hence possible transport to the southwest. Another remarkable observation to emerge from the data is that the average NO$_2$ near-surface mixing ratios at 350 nm are greater than the 450 and 560 nm ones, which is exploited in the onion-peeling approach (Sect. 4.3).

To quantitatively assess azimuth inhomogeneity, the relative azimuth asymmetry (RAA) is introduced here. The RAA is defined as $(1-[NO_{2,min} / NO_{2,max}])$, where NO$_{2,min}$ and NO$_{2,max}$ are the minimum and maximum mixing ratios of NO$_2$ obtained within a period of time. The RAA calculated for the early morning, midday, afternoon, and evening are 68 ± 7, 34 ± 4, 63 ± 4, and 28 ± 6 %, respectively. This variability is independent of the wavelength and reflects that similar changes are probed by the three different effective path lengths, most likely due to changes in NO$_2$ emissions close to the city of Mainz. Similarly, the relative longitudinal asymmetry (RLA) is defined as $(1-[NO_{2,min} / NO_{2,max}])$, but with the NO$_{2,min}$ and NO$_{2,max}$ taken with a constant AA and for a period of time of 1.5–2 h. For example, the RLA for the standard AA is 41 % (360 nm), 13 % (450 nm), and 11 % (560 nm) during the early morning (07:30–09:00). In this case there is a strong wavelength dependence confirming that major emissions are released close to the city of Mainz and transported to the southwest. In contrast to the early morning, midday values of RLA are lower than 7 % for the three wavelengths, hence are more homogeneous air mass along the same line of sight. Although the RLA may vary slightly for different AAs, the same behavior described before was found for all of the AAs for the same period of time.

Figure 7. Azimuthal diurnal variation of **(a)** correction factors (f_c), **(b)** differential effective path length (L_{eff}, see Eq. 7), and **(c)** NO$_2$ near-surface VMRs at 360, 450, and 560 nm (left to right). The radii represent the local time, and the color scale the magnitude of the f_c, L_{eff}, and NO$_2$ VMR, using the same color scale at the three wavelengths.

Table 6. Overview of the most important errors in the determination of NO$_2$ VMR in both the OE and parameterization method.

Method	Error overview (%)	Total error (%)
OE	Noise: ~ 5; Smoothing: ~ 7; Forward model: ~ 10	~ 13–16^*
Parameterization	Fit error: ~ 5; correction factor: ~ 10	~ 12–15

* Representative of layers close to the surface (< 0.6 km).

4.2.2 Uncertainties of NO$_2$ vertical profiles and near-surface VMR

Table 6 shows a summary of the errors for both OE and parameterization. In the following, the errors of the vertical profile retrievals by OE are discussed briefly. For a detailed and more formal description of the error associated in the retrieval of vertical profile using OE we refer to the excellent studies by Rodgers (1990, 2000) and Steck (2002). We have considered three main errors: (1) retrieval noise error associated with the uncertainty in the dSCD; (2) the smoothing error, which represents how in average the constrained retrieval differs from the true state due to the vertical smoothing; and (3) systematic errors from the forward model parameters. The retrieval noise is so far the easiest error to be determined since it is retrieved directly from the gain matrix ($\mathbf{G_y}$) and the $\mathbf{S_\varepsilon}$ covariance matrix error as $\mathbf{S_n} = \mathbf{G_y} \mathbf{S_\varepsilon} \mathbf{G_y^T}$. As mentioned before $\mathbf{S_\varepsilon}$ is built using the square of the DOAS fit error, which represents a final error of less than 1 %; however the final noise error considers uncertainties in the NO$_2$ absorption cross section (~ 5 %). The error due to smoothing and the forward model covariance matrices listed in Table 6 were taken from sensitivity studies. The smoothing error is determined based on the inversion with simulated NO$_2$ dSCDs. First, simulated NO$_2$ dSCDs under pre-defined scenarios were used to retrieve the NO$_2$ vertical profiles under known conditions. The difference between the "real" and the retrieved NO$_2$ profiles was taken as an estimate of this error. On the other hand the forward model parameters are esti-
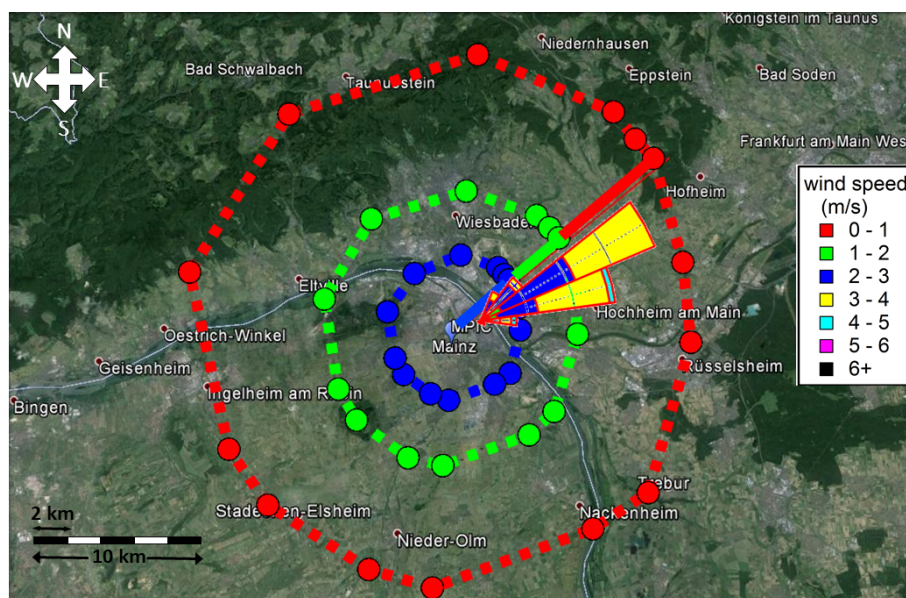
Figure 8. Map of the surroundings around the city of Mainz, Germany. The circles represent the MAX-DOAS spatial scales probed in different azimuth directions, and at different wavelengths: blue – the average L_{eff} determined for the 2° EA at 350 nm; green – 477 nm; red – 577 nm at noon on 17 June 2013. The solid line in azimuth direction of 50.8 represents the "standard" AA where the EA scans were performed. The diurnal azimuth distribution of wind speed is also shown.

mated by changing the most important input parameters such as aerosol optical properties in an expected range. In general, lower error was found for layers close to the surface (below 0.6 km). At higher altitudes, the smoothing error is higher; hence the total error increases due to lack of sensitivity and uncertainties in the aerosol profiles.

The error of the parameterization approach to derive near-surface NO$_2$ VMR is estimated by an error propagation of the inputs to Eq. (5). There are two main factors contributing to the final error: (1) error in the analysis of NO$_2$ and O$_4$ dSCD, and (2) error in the correction factor f_c. The typical root mean square (RMS) residual achieved in the fit of NO$_2$ and O$_4$ is on the order of 4.5×10^{-4}, 3.5×10^{-4}, and 3×10^{-4} for the 360, 450, and 560 nm fits, respectively; lower RMS was observed on other days when the NO$_2$ concentrations were lower. These noise levels correspond roughly to 2–3 times the fit error in the DOAS analysis. We use a 2-sigma fit error for the error propagation in the dSCD of NO$_2$ and O$_4$ in Eq. (5). As mentioned in Sect. 3.2.3 the error in the correction factor takes into account the variations due to uncertainties in the MLH$_{NO_2}$ and aerosol optical properties. Table 5 shows the main input parameters that are varied in order to estimate the variability of the correction factor. Figure S2 shows the O$_4$ dSCD, O$_4$ dAMF, and f_c binned by SRAA for different SZA. In this figure the error bars represent the uncertainty estimated using the overall range of variability derived from the above sensitivity studies. The uncertainty of the correction factors is below 10 % most of the time, and for the three wavelengths there is a systematic pattern visible in that the

strongest SRAA effects occur at SZAs between 40 and 70°. Similar findings were observed in Sinreich et al. (2013). The error is normally greater in the 360 nm data than in the data for visible wavelengths. The final error of the VMR is between 12 and 15 %.

4.3 Range-resolved NO$_2$ azimuth dependencies (onion peeling)

In order to distinguish the NO$_2$ from different air masses, we applied the onion-peeling approach introduced in Sect. 3.3. The azimuthal diurnal cycles of NO$_2$ calculated with Eq. (7) for the different distances are shown in Fig. 9. The NO$_2$ close to the site (VMR$_1$) is determined with the 350 nm values; the difference in VMR calculated between the 450 and 350 nm values, and 560 and 450 nm values weighted by their path lengths are denoted with VMR$_2$ and VMR$_3$ (see Eq. 8). Note that the color code scales are different for each range to better visualize the azimuthal distribution. The range-resolved NO$_2$ VMR shows a definitive azimuth inhomogeneity for the three different distances probed. As mentioned before there is an enhancement of NO$_2$ VMR$_1$ in the west quadrant which may be associated with the local NO$_2$ transport from the cities of Wiesbaden and Mainz in agreement with the wind patterns in Fig. 8, especially in the morning. Surprisingly this enhancement is not seen in the VMR$_2$ and VMR$_3$ in the morning: instead they increase in the afternoon likely due to transport. The overall error is obtained using the error propagation in Eq. (8) (see Fig. S3).

The RAA and RLA (Sect. 4.2.1) were estimated for each ring accessible in the onion-peeling approach. In this case, the RAA for the inner ring (RAA_{VMR1}) in the early morning is the same as in Sect. 4.2.1 (68 ± 7 %). On the other hand, the RAA in the second ring (RAA_{VMR2}) is 76 ± 6 %, a slightly higher value than the inner ring. Interestingly, the RAA of the outermost ring (RAA_{VMR3}) decreases with a value of 38 ± 15 %, confirming transport from the cities of Mainz and Wiesbaden to the second ring has diluted in the third ring. Additionally, the RLA is estimated for each ring at fixed AA (at the same time). For example, the RLA between ring 2 and 3 (RLA_{VMR2-3}) is only 11 ± 5 % for the 50.8° AA; however the RLA_{VMR2-3} is 71 ± 6 % for the 281° AA in the early morning. In general these data indicate that emission sources from the city of Mainz are being transported to the southwest in the early morning.

4.4   Azimuth distribution of R_{FN}, R_{GN}, and R_{GF}

We investigate the azimuthal diurnal distribution of R_{FN}, R_{GN}, and R_{GF} as measures for the chemical state of the atmosphere (photochemical radical production, O_3 production rates, VOC vs. NO_x limitation in O_3 production rates). The variation of the ratios in the boundary layer is obtained using dSCD measured with an EA of 2°. Similar to the NO_2 we present results for the case study in Fig. 10. Duncan et al. (2010) characterized the relationship between R_{FN} and O_3 production in Los Angeles and suggested three different regimes: the VOC-limited regime when the $R_{FN} < 1$, the NO_x-limited regime for $R_{FN} > 2$, and the transition regime between 1 and 2. This was determined by means of modeling studies in the troposphere and confirmed by tropospheric HCHO and NO_2 vertical column density ratios from the OMI satellite instrument. During MAD-CAT, the morning values for R_{FN} are typically lower than 1 for all directions, followed by a sharp increase reaching values larger than 1. Interestingly, only in the south values up to 2 are observed. The variability in R_{FN} indicates that 2-D-MAX-DOAS can provide useful information to constrain the azimuthal gradients in the rate of O_3 production.

In reviewing the literature, no data were found on the association of CHOCHO-to-NO_2 ratios (R_{GN}) as an indicator of photochemical radical production. The R_{GN} diurnal variation is shown in Fig. 10b, and R_{GN} is found to exhibit a similar behavior to R_{FN}. Hence, we hypothesize that information on radical production and O_3 formation rates is also constrained by R_{GN}. From the data in Fig. 7c, it is apparent that there is a decrease in the NO_2 in the south at the same times; therefore the enhancements observed in R_{FN} and R_{GN} are probably largely driven by the decrease in NO_2.

The R_{GF} ratio has been suggested as an indicator for the relative contribution of biogenic and/or anthropogenic VOC sources to O_3 and aerosol formation (Vrekoussis et al., 2010; DiGangi et al., 2012). Figure 10c shows the azimuthal diurnal variation of R_{GF}. Contrary to the diurnal pattern of R_{FN}

and R_{GN}, the R_{GF} does not show a diurnal cycle and there is no apparent sharp increase in the early afternoon. For most of the daytime the R_{GF} remains steady with values lower than 0.02. Interestingly, changes in HCHO and CHOCHO do not affect the ratio, likely indicating similar sources from primary emissions and secondary (photochemical) sources. Satellite studies such as Vrekoussis et al. (2010) reported that for R_{GF} lower than 0.04 the air mass is associated with anthropogenic VOC emission sources while indices above 0.04 might relate to biogenic emission sources. Recently, Di-Gangi et al. (2012) reported some discrepancies with satellites, where R_{GF} values below 0.04 were calculated in environments dominated by biogenic emissions. The error in the ratios, calculated with the DOAS fit error propagation of the dSCDs, show errors lower than 5, 10, and 20 % for R_{FN}, R_{GN}, and R_{GF}, respectively. Our results in this work, based on urban measurements carried out in Mainz, Germany, show agreement with values reported by satellites and indicate the dominance of anthropogenic influences in Mainz, Germany.

4.5   Comparison with OMI NO_2 VCD

The variability in spatial scales probed by the different wavelengths at variable AA provides a novel perspective on the comparison with satellites. The sensitivity in the apparent NO_2 VCD as seen from space to the ground resolution is well documented (Beirle et al., 2004; Boersma et al., 2007; Fioletov et al., 2013); the maximum NO_2 VCD increases strongly as the spatial scales that are being probed approach the sizes of cities (e.g., Beirle et al., 2004, 2011). Questions about the inhomogeneity in NO_2 VCD near urban hot spots pose challenges to assessing the meaning of satellite measurements; a lack of measurements to constrain these distributions further poses challenges to compare measurements and atmospheric model predictions.

We have calculated the average NO_2 VCDs in the azimuth sectors located to the north and south of the measurement site. The average VMR obtained with the full azimuth scan and the three different wavelengths are converted into VCD using the MLH_{NO_2} calculated previously. During the OMI overpass (12:20 LT) there are two pixels of 15×30 km that can be used for the comparison, southeast and northwest sections (see Fig. S3). Figure 11 shows the NO_2 VCD comparison retrieved at three different wavelengths and for the two pixels probed with the OMI NO_2 VCD from DOMINO version 2.0. The comparison shows a better agreement using the 560 nm VCD rather than using 450 and 350 nm. At the top of Fig. 11 the area of the total azimuth scan and the two pixels from OMI are shown. The spatial scales covered at the three different wavelengths represent approximately 10 % (350 nm), 44 % (450 nm), and 140 % (560 nm) of the footprint probed under near-nadir geometries by the OMI instrument onboard the EOS-Aura satellite (Boersma et al., 2007). The agreement shows a strong dependence on the spatial resolution. Differences larger than a factor of 2 at 350 nm are
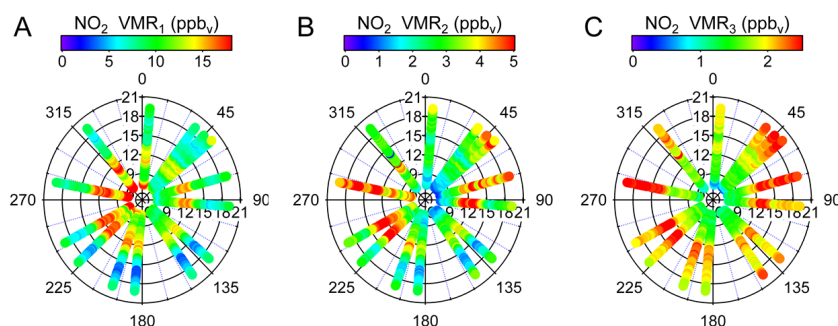
Figure 9. Azimuth dependence of the NO_2 VMR diurnal cycle at the three distances accessible to the onion-peeling approach. The NO_2 in the vicinity of the site (VMR_1) is determined at 360 nm; for calculations of the NO_2 VMR_2 and VMR_3 see Eq. (8) and text for details.
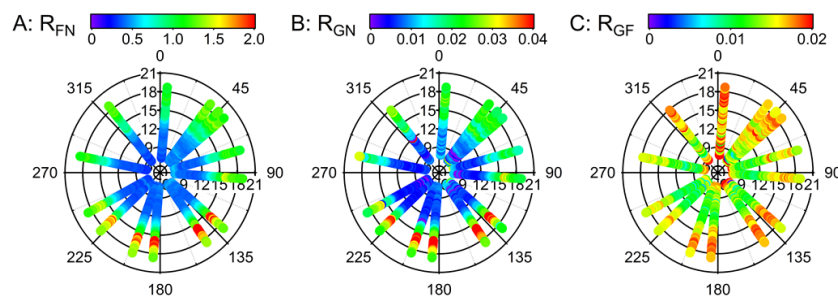

Figure 10. Azimuth dependence of the time series of the trace gas ratios R_{FN}, R_{GN}, and R_{GF} on 17 June 2013. See text for details.

greatly reduced at the longer wavelengths, and agreement is better than 20 % at 560 nm. The error bars in the NO_2 wavelength dependence represent the NO_2 VCD standard deviation calculated based on the azimuth distribution, and the OMI error bars are the errors in the NO_2 VCD reported during the overpass. Notably, the best agreement is observed when the spatial scales most closely resemble each other, reflecting the importance of matching spatial scales. Note that, even though the error of the OMI-based NO_2 is quite large due to the single overpass, the overestimation of the MAX-DOAS obtained in the UV is still significant. Further research should be done to investigate the azimuth distribution and wavelength dependence with long time series. It is interesting to note that the assumption made to calculate the azimuth NO_2 VCD using the azimuthal NO_2 VMR would be overestimated based on the NO_2 vertical profiles (Fig.6), which are not box profile type. To establish the possible overestimation, we performed a sensitivity study where the NO_2 VCD in the standard azimuth view was calculated integrating the NO_2 vertical profiles, and we compare them with the assumption of using the MLH_{NO_2} estimated previously. As expected, the NO_2 VCD is overestimated by a factor of 15–20 % if we use the assumption of the MLH_{NO_2}. In this context, the agreement of the NO_2 VCD at 560 nm would be even better, and the overestimation of the 350 and 450 nm NO_2 VCD would be on the order of 35 and 25 %, respectively.

Oetjen et al. (2013) compared an extensive data set of highly spatially resolved tropospheric NO_2 VCD measured

with the CU airborne MAX-DOAS instrument (CU AMAX-DOAS; about 1 km resolution, 22 000 individual measurements) with coincident OMI VCD over California. They showed that better correlations are observed upon filtering their data for conditions when a larger area and more meaningful fraction of the OMI ground pixel had been sampled. However, for large OMI pixels that included relatively large unpolluted areas, they found a tendency for underestimation in the OMI measurements. Furthermore, past NO_2 VCD comparisons have shown an underestimation (up to 40 %) by satellites with respect to ground-based MAX-DOAS (Brinksma et al., 2008; Ma et al., 2013; Kanaya et al., 2014). Brinksma et al. (2008) have shown that MAX-DOAS measurements with a single azimuth angle might not be appropriate for comparison with satellites since the representation of the air mass may be different. For this particular case study, Fig. 11 shows that the directionality and footprint achieved with 2-D-MAX-DOAS can be used to better compare with satellites. Efficient means to sample and assess spatial gradients/inhomogeneities and horizontal/vertical distributions are increasingly important as future satellite missions from geostationary orbit (TEMPO, Sentinel 4 etc.) will track the chemical composition with high temporal and spatial resolution.
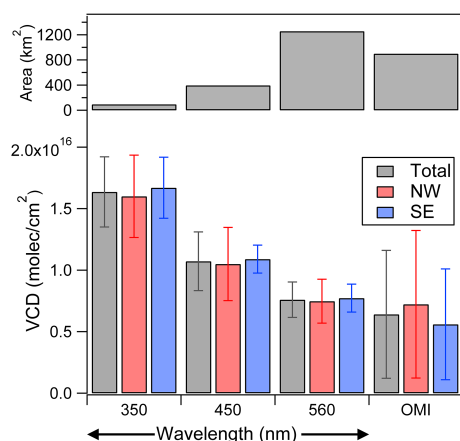
Figure 11. Comparison between the NO_2 VCD obtained at the three wavelengths with the NO_2 VCD measured by OMI, for two OMI pixels located to the NW and SE of the site during the OMI overpass on 17 June 2013. The area probed by the azimuth scan at each wavelength and the OMI pixels is represented on top.

4.6 Validating 3-D measurements

The RTM parameterization approach to convert dSCDs into near-surface VMR used in this study has previously been compared with independent validation data for NO_2 (Sinreich et al., 2013) and glyoxal (Volkamer et al., 2015). We refer to Fig. 7a of Sinreich et al. (2013) that compared the near-surface NO_2 VMRs from the RTM parameterization in three different azimuth views by means of two co-located long-path (LP-) DOAS instruments (facing in opposite directions) in Mexico City. In that particular case, there was a generally good agreement of NO_2 between the two methods, although differences were found when the air mass probed was different for the two LP-DOAS instruments, indicating strong NO_2 concentration gradients in air surrounding the site. For glyoxal, the near-surface VMR from Ship MAX-DOAS was compared with in situ cavity-enhanced DOAS (CE-DOAS) and airborne MAX-DOAS (AMAX-DOAS) over the remote tropical eastern Pacific Ocean (Volkamer et al., 2015). In this case, the RTM parameterization was applied to glyoxal dSCDs measured by the Ship MAX-DOAS using EA of $+1.5$, which is slightly lower than but similar to the EA used in this study. The in situ glyoxal, ozone, and other measurements on the ship are constant over the course of several hours (Coburn et al., 2014) and indicate homogeneous air during this case study. Under such conditions good agreement (within 10 %) was observed between in situ CE-DOAS and Ship MAX-DOAS measurements of glyoxal near-surface VMR (see Sect. 3.4 and Fig. 8 in Volkamer et al., 2015).

The comparison with OMI data in Sect. 4.5 is not meant as an attempt at validation. Rather the better agreement found for the comparison of data sampled on similar spatial scales poses questions as how to best validate 2-D-MAX-DOAS ob-

servations (and satellites) under conditions when the air is inhomogeneous. In Sect. 4.6.1 we compare the NO_2 VMR from OE and parameterization in an attempt to assess different retrieval approaches of dSCDs that were generally measured in the same general direction (fixed AA direction of the standard view) but are nonetheless not identical. Section 4.6.2 then discusses the challenges with validating 3-D distributions of NO_2 and other gases in inhomogeneous air that need to be actively addressed to achieve the best results from ongoing and future comparison efforts.

4.6.1 Comparison of near-surface NO_2 VMRs: OE and parameterization

The multi-wavelength NO_2 near-surface VMRs retrieved with the parameterization approach are compared with those derived from OE for the standard azimuth view in Fig. S5. Note that the two approaches are independent and in particular do not use identical NO_2 dSCDs. As pointed out in Sects. 3.2.3 and 3.3 the NO_2 derived with the parameterization approach uses only data from the lowest EA, and the mixing ratio is characteristic only over the differential effective path length and height in the lower portion of the MLH. By contrast, the OE uses NO_2 dSCDs from a full set of EAs. In reality, the comparison of MLH_{NO_2} in Sect. 4.1.2 shows that there is some variability in NO_2 with altitude. The near-surface VMR is subject to smoothness and assumptions about a priori profile shape/magnitude and error covariance matrices, and thus differences in Fig. S5 may represent actual gradients in the chemical state of the atmosphere and should not be interpreted exclusively as an "error" of the retrieval strategy. In order to account for the different horizontal range sensitivity we have averaged the NO_2 profiles from Fig. 6 to a similar representative height of the parameterization approach for each wavelength. In general, both methods capture the NO_2 variability within the spatial scale for each wavelength. The slopes of linear regressions (parameterization versus OE) varied from 0.83 to 0.88, and intercepts from 0.11 to 1.76 ppbv NO_2 (see insert on Fig. S5). There is further generally good correlation, with the R^2 ranging between 0.55 and 0.78, for each wavelength considering the difference in sensitivity of air masses probed by the two methods.

4.6.2 Challenges with validating 3-D distributions

The gradients in NO_2 identified in this work pose the question of how 3-D measurements can be best validated. Figure 11 emphasizes the relevance of this question in the context of comparable instrument footprint and satellite ground pixel size. Our measurements show that NO_2 near-surface mixing ratios vary by a factor of larger than 3 in different azimuth directions, and by up to a factor of 1.5–2 at fixed AA (Sect. 4.2.1). The true NO_2 variability is likely higher, since our measurements inherently average over between 5 and 30 km horizontal distance (Sect. 4.2).

The regional air quality network in Mainz provides in situ NO_2 measurements. A comparison with our 3-D distributions is not straightforward and has not been attempted for at least two reasons: (1) previous comparison of NO_2 and HCHO in situ observations and open-path spectroscopic measurements show a rather fair level of correlation $(0.32 < R^2 < 0.77)$ in ambient air (Harder et al., 1997; Cárdenas et al., 2000; Jimenez et al., 2000; Kim et al., 2001; Thornton et al., 2003; Dunlea et al., 2007), while comparisons under controlled conditions show excellent correlation (also for ambient air) if the air is well mixed $(R^2 > 0.98)$ (Thalman et al., 2015). The comparison with network sensors thus is unlikely to carry much meaning in light of the different air masses probed. The inhomogeneity along a constant AA is 50–100 %, and a lower limit for the actual inhomogeneity given the averaging nature of 2-D-MAX-DOAS measurements. Any better agreement would be coincidental. Moreover, this fundamental sampling problem is not unique to a comparison with in situ sensors. For example, car MAX-DOAS measurements have the benefit of integrating vertically but are conducted in air that is offset horizontally from the measurement site of the 2-D-MAX-DOAS and is also subject to the inhomogeneity along a constant AA. (2) Additional artifacts can arise with in situ sensors that measure NO_2 indirectly; e.g., molybdenum converters (as used in the Mainz city network) suffer from interferences of NO_y species that high-bias the sensor signal attributed to NO_2 (Dunlea et al., 2007; Villena et al., 2012). For example, Villena et al. (2012) found that values of NO_2 can be overestimated by up to a factor of 4 using molybdenum converters. On the other hand, photolytic converters can show even stronger negative interferences than the molybdenum converters, especially under high pollution levels (high NO_x concentrations) (Villena et al., 2012). The sensors used to validate 3-D NO_2 distributions should be chosen to actively avoid such potential for bias. In order to validate azimuth distributions of NO_2, a first step consists in comparing the NO_2 SCDs from multiple 2-D-MAX-DOAS instruments during the MAD-CAT campaign. An according manuscript is currently in preparation for azimuthal distribution of NO_2 (Remmers et al., 2015). Additionally, upcoming studies regarding comparison of HONO and CHOCHO dSCD from various instruments have been projected (Ortega et al., 2015a; Wang et al., 2015). The subsequent validation of 3-D distributions of NO_2 is non-trivial. In particular, the heterogeneity of NO_2 poses the following challenges to designing a sampling strategy for retrieval validation.

The 3-D mapping of the true NO_2 variability in an air volume of $\sim 1000\,km^3$ that is probed by the CU 2-D-MAX-DOAS instrument near instantaneously by means of in situ sensors on aircraft would require a fast and flexible airplane. A challenge exists in the fact that the atmospheric state of NO_2 is likely changing on the timescales needed to map such an air volume with in situ sensors on aircraft. At a typical airspeed of small aircraft, it would take 3–4 h to map a box

of dimensions $32 \times 32 \times 1\,km$ ($\sim 1000\,km^3$) by traverses at distances that are 1 km apart and are flown at a single altitude; however, the variations in the atmospheric state are likely significant as times exceed 30 min (M. Trainer, personal communication, 2010). It would therefore be desirable to have multiple aircraft. Multiple aircraft would have the added benefit that independent vertical profile information could be obtained effectively. The complementary validation by highly time-resolved NO_2 column observations from cars (Shaiganfar et al., 2011) and aircraft (Oetjen et al., 2013) provide cost-effective means to access larger air volumes. The retrievals are reasonably straightforward and robust, and have been successfully employed for satellite validation (Oetjen et al., 2013). Imaging spectrometers on the ground (Lohberger et al., 2004) and push broom/whisk broom scanner techniques on aircraft (Kowalewski and Janz, 2009; Heue et al., 2008; General et al., 2014) hold great promise to provide information on finer scales. While imaging techniques greatly increase the amount of information that can be obtained from a single instrument/platform, the quantification of these data is not free of challenges that warrant independent assessments. Ideally, future attempts to validate 3-D distributions will use a combination of multiple aircraft and a combination of active and passive remote sensing of NO_2, including networks of ground-based remote-sensing and in situ sensors (Ryerson et al., 2013), and will be further coordinated with measurements from mobile platforms, including in situ measurements from vans and aircraft, car MAX-DOAS, nadir mapping and push-broom imaging from aircraft, and NO_2 lidars (Volten et al., 2009; Vlemmix et al., 2011). Such efforts should be supported by atmospheric models to inform the best sampling strategy and bridge between the various spatial scales probed by these diverse available measurements to probe 3-D distributions of NO_2. State-of-the-art atmospheric models currently predict NO_2 with a resolution of $4\,km \times 4\,km$, which is sufficient to represent broad spatial features such as those measured by 2-D-MAX-DOAS. However, this resolution would be insufficient to resolve the spatial gradients in NO_2 that can be expected near the edges of street canyons or highways, which can pose challenges if the complementary information derived from in situ sensors and column observations is to be integrated by models. The location for future attempts to validate 3-D distributions of NO_2 should include homogeneous yet variable NO_2 for best results.

5 Summary and conclusions

We introduce the CU 2-D-MAX-DOAS instrument and present a retrieval to conduct measurements of NO_2 near the surface in three dimensions, as well as measure azimuth dependences in trace gas ratios that are indicators for the rate of O_3 and aerosol formation. Our retrieval builds on and im-

proves upon Sinreich et al. (2013). We conclude the following:

- The uncertainty from parameterization of radiative transfer (RT) is greatly reduced by knowledge of the mixing height of NO_2 (MLH_{NO_2}), which is estimated by means of the measured vertical distribution of NO_2. The comprehensive mapping of the correction factors as a function of geometry suggests that under certain conditions (small solar relative AA) uncertainties with calculating correction factors can become limited by the knowledge of how well RT models (RTMs) represent O_4 dAMFs. This warrants further investigation.

- The time resolution of our fast 2-D-MAX-DOAS measurements (here 14 min) for a complete 360° azimuth view is deemed sufficient to document changes in the atmospheric distributions of NO_2, HCHO, and CHOCHO that occur on 30 min or longer timescales. For future 2-D-MAX-DOAS measurements we recommend the use of more than one azimuth view to estimate the MLH_{NO_2} in several directions and account for possible terrain effects.

- Range-resolved azimuthal distributions of NO_2 have been derived for the first time to our knowledge using a 2-D-MAX-DOAS technique, and there is potential to map NO_2 horizontal distributions with sub-parts-per-billion detection accuracy over spatial scales that range from a few kilometers up to 30 km distance from the measurement site.

2-D-MAX-DOAS can serve to better constrain and test the spatial scales over which trace gases vary in the atmosphere. This information is useful to document and better map the chemical state of the atmosphere. In particular, we observe the following during MAD-CAT:

- Azimuth and longitudinal distributions of NO_2 reveal gradients that vary as a function of time of day. The largest gradients are observed in the early morning in accordance with the RAA and RLA introduced in Sect. 4.2.1. The RAA is 68 ± 7, 34 ± 4, 63 ± 4, and 28 ± 6 % in the early morning, midday, afternoon, and evening, respectively. The azimuth variation in the morning (highest NO_2 in the west, lowest in the east) is different from that in the afternoon (higher NO_2 in the north, lowest NO_2 in the south). Similar variability is found for the three different wavelengths. Similarly, the RLA is higher in the early morning, with differences of up to 1.5–2 within the same azimuth view.

- The RAA and RLA for the different areas probed with onion peeling confirm transport of NO_2 from Mainz and Wiesbaden to the southwest, reaching horizontal length of up to 25 km but decreasing after that according to the decrease of RLA in the outermost ring.

- Generally the trace gas ratios formaldehyde to NO_2 (R_{FN}) and glyoxal to NO_2 (R_{GN}) show a more homogeneous azimuth distribution than NO_2. However we identified high differences in the afternoon where the RAA is 53 ± 10 %, which corresponds to a factor of 2 times higher ratios towards the south.

- R_{FN} ratios have been proposed to inform VOC vs. NO_x control of O_3 formation rates (Duncan et al., 2010). Our measurements suggest that R_{GN} is similar to R_{FN} and holds complementary information, because it constrains O_3 production rates at different spatial scales (longer wavelengths). The integration with atmospheric models will benefit from design of instrument masks that average model output to match the observations.

- OVOC ratios (glyoxal to formaldehyde, R_{GF}) are always below 0.04 in all azimuth directions. This is indicative of anthropogenic VOC influences dominating around the site. Nevertheless, the RAA can vary by up to a factor of 2 with maximum values toward the northeast and minimum towards the west. This ratio holds potential to distinguish anthropogenic and biogenic influences on oxidative capacity, O_3 production, and aerosol production rates.

Finally, we characterize the spatial scales probed by 2-D-MAX-DOAS at different wavelengths to represent a mean area of 150, 600, and 1960 km^2 at 350, 450 and 570 nm, respectively. These scales fill a gap in the spatial scales predicted by atmospheric models (e.g., 4 km × 4 km by WRF-Chem, CAMx) and probed by satellites (e.g., several hundreds to thousands of square kilometers). It is shown that variations in the chemical composition of the atmosphere on spatial scales smaller and larger than those probed by satellites can be tracked by 2-D-MAX-DOAS. The azimuthal and the ground-resolution variability can play an important role in the validation process of ongoing measurements onboard satellites (OMI, SCHIAMACHY, GOME-2) and future hourly satellite measurements (GEMS, TEMPO). Azimuth-dependent information therefore holds potential to better constrain atmospheric models and better understand the information obtained by satellites and models. This is exemplified by a case study comparison of two ground pixels of the OMI satellite: at the differential effective path length realized with the 560 nm, and averaging over a full azimuth scan, NO_2 VCDs show a good agreement with OMI (within 20 %). This is attributed to the similarity between the 560 nm footprint and that probed by OMI, while using the 350 and 450 nm data would result in an overestimation of the OMI VCD by 60 and 40 %, respectively.

Appendix A: List of frequently used abbreviations

2-D	2-dimensional
AA	azimuth angle
AERONET	AErosol RObotic NETwork
AMF	air mass factor
AOD	aerosol optical depth
CHOCHO	glyoxal
CU	University of Colorado
dAMF	differential air mass factor
DOAS	differential optical absorption spectroscopy
DOF	degrees of freedom
dSCD	differential slant column density
EA	elevation angle
FOV	field of view
FWHM	full width at half maximum
HCHO	formaldehyde
LT	local time
MAD-CAT	multi-axis DOAS comparison campaign for aerosols and trace gases
MAX-DOAS	multi-aXis DOAS
McArtim	Monte Carlo Radiative Transfer Model
MPIC	Max Planck Institute for Chemistry
NO_2	nitrogen dioxide
O_4	oxygen collision pair, O_2-O_2
OE	optimal estimation
OMI	Ozone Monitoring Instrument
OVOC	oxygenated volatile organic compound
PBL	planetary boundary layer
ppbv	parts per billion by volume; $1\,\text{ppbv} = 2.2 \times 10^{10}$
RAA	relative azimuth asymmetry
R_{FN}	formaldehyde (HCHO)-to-nitrogen-dioxide (NO_2) ratio
R_{GF}	glyoxal (CHOCHO)-to-formaldehyde (HCHO) ratio
R_{GN}	glyoxal (CHOCHO)-to-nitrogen-dioxide (NO_2) ratio
RLA	relative longitudinal asymmetry
RTM	radiative transfer model
RMS	root mean square
SA	surface albedo
SOA	secondary organic aerosol
SRAA	solar relative azimuth angle
SSA	single scattering albedo
SZA	solar zenith angle
VCD	vertical column density
VMR	volume mixing ratio
VOC	volatile organic compound

The Supplement related to this article is available online at doi:10.5194/amt-8-2371-2015-supplement.

Edited by: M. Van Roozendael

References

Baidar, S., Oetjen, H., Coburn, S., Dix, B., Ortega, I., Sinreich, R., and Volkamer, R.: The CU Airborne MAX-DOAS instrument: vertical profiling of aerosol extinction and trace gases, Atmos. Meas. Tech., 6, 719–739, doi:10.5194/amt-6-719-2013, 2013.

Barnard, J. C., Volkamer, R., and Kassianov, E. I.: Estimation of the mass absorption cross section of the organic carbon component of aerosols in the Mexico City Metropolitan Area, Atmos. Chem. Phys., 8, 6665–6679, doi:10.5194/acp-8-6665-2008, 2008.

Barret, B., De Mazière, M., and Mahieu, E.: Ground-based FTIR measurements of CO from the Jungfraujoch: characterisation and comparison with in situ surface and MOPITT data, Atmos. Chem. Phys., 3, 2217–2223, doi:10.5194/acp-3-2217-2003, 2003.

Beirle, S., Platt, U., Wenig, M., and Wagner, T.: Highly resolved global distribution of tropospheric NO_2 using GOME narrow swath mode data, Atmos. Chem. Phys., 4, 1913–1924, doi:10.5194/acp-4-1913-2004, 2004.

Beirle, S., Boersma, K. F., Platt, U., Lawrence, M. G., and Wagner, T.: Megacity Emissions and Lifetimes of Nitrogen Oxides Probed from Space, Science, 333, 6050, doi:10.1126/science.1207824, 2011.

Boersma, K. F., Eskes, H. J., Veefkind, J. P., Brinksma, E. J., van der A, R. J., Sneep, M., van den Oord, G. H. J., Levelt, P. F., Stammes, P., Gleason, J. F., and Bucsela, E. J.: Near-real time retrieval of tropospheric NO2 from OMI, Atmos. Chem. Phys., 7, 2103–2118, doi:10.5194/acp-7-2103-2007, 2007.

Bogumil, K., Orphal, J., Homann, T., Voigt, S., Spietz, P., Fleischmann, O., Vogel, A., Hartmann, M., Kromminga, H., Bovensmann, H., Frerick, J., and Burrows, J.: Measurements of molecular absorption spectra with the SCIAMACHY pre-flight model: instrument characterization and reference data for atmospheric remote-sensing in the 2302380 nm region, J. Photoch. Photobio. A, 157, 167–184, doi:10.1016/S1010-6030(03)00062-5, 2003.

Brinksma, E. J., Pinardi, G., Volten, H., Braak, R., Richter, A., Schönhardt, A., van Roozendael, M., Fayt, C., Hermans, C., Dirksen, R. J., Vlemmix, T., Berkhout, A. J. C., Swart, D. P. J., Oetjen, H., Wittrock, F., Wagner, T., Ibrahim, O. W., de Leeuw, G., Moerman, M., Curier, R. L., Celarier, E. A., Cede, A., Knap, W. H., Veefkind, J. P., Eskes, H. J., Allaart, M., Rothe, R., Piters, A. J. M., and Levelt, P. F.: The 2005 and 2006 DANDELIONS NO_2 and aerosol intercomparison campaigns, J. Geophys. Res., 113, D16S46, doi:10.1029/2007JD008808, 2008.

Cárdenas, L. M., Brassington, D. J., Allan, B. J., Coe, H., Alicke, B., Platt, U., Wilson, K. M., Plane, J. M., and Penkett, S. A.: Intercomparison of formaldehyde measurements in clean and polluted atmospheres, J. Atmos. Chem., 37, 53–80, 2000.

Chance, K. V. and Spurr, R. J. D.: Ring effect studies: Rayleigh scattering, including molecular parameters for rotational Raman scattering, and the Fraunhofer spectrum, Appl. Opt., 36, 5224–5230, doi:10.1364/AO.36.005224, 1997.

Clémer, K., Van Roozendael, M., Fayt, C., Hendrick, F., Hermans, C., Pinardi, G., Spurr, R., Wang, P., and De Mazière, M.: Multiple wavelength retrieval of tropospheric aerosol optical properties from MAXDOAS measurements in Beijing, Atmos. Meas. Tech., 3, 863–878, doi:10.5194/amt-3-863-2010, 2010.

Coburn, S., Dix, B., Sinreich, R., and Volkamer, R.: The CU ground MAX-DOAS instrument: characterization of RMS noise limitations and first measurements near Pensacola, FL of BrO, IO, and CHOCHO, Atmos. Meas. Tech., 4, 2421–2439, doi:10.5194/amt-4-2421-2011, 2011.

Coburn, S., Ortega, I., Thalman, R., Blomquist, B., Fairall, C. W., and Volkamer, R.: Measurements of diurnal variations and eddy covariance (EC) fluxes of glyoxal in the tropical marine boundary layer: description of the Fast LED-CE-DOAS instrument, Atmos. Meas. Tech., 7, 3579–3595, doi:10.5194/amt-7-3579-2014, 2014.

Deutschmann, T., Beirle, S., Frieß, U., Grzegorski, M., Kern, C., Kritten, L., Platt, U., Prados-Roman, C., Puckimacrte, J., Wagner, T.,Werner, B., and Pfeilsticker, K.: The Monte Carlo atmospheric radiative transfer model McArtim: Introduction and validation of Jacobians and 3-D features, J. Quant. Spectrosc. Radiat. Transfer, 112, 1119–1137, doi:10.1016/j.jqsrt.2010.12.009, 2011.

DiGangi, J. P., Henry, S. B., Kammrath, A., Boyle, E. S., Kaser, L., Schnitzhofer, R., Graus, M., Turnipseed, A., Park, J-H., Weber, R. J., Hornbrook, R. S., Cantrell, C. A., Maudlin III, R. L., Kim, S., Nakashima, Y., Wolfe, G. M., Kajii, Y., Apel, E.C., Goldstein, A. H., Guenther, A., Karl, T., Hansel, A., and Keutsch, F. N.: Observations of glyoxal and formaldehyde as metrics for the anthropogenic impact on rural photochemistry, Atmos. Chem. Phys., 12, 9529–9543, doi:10.5194/acp-12-9529-2012, 2012.

Dix, B., Baidar, S., Bresch, J. F., Hall, S. R., Schmidt, K. S., Wang, S., and Volkamer, R.: Detection of iodine monoxide in the tropical free troposphere, P. Natl. Acad. Sci. USA, 110, 2035–2040, doi:10.1073/pnas.1212386110, 2013.

Duncan, B. N., Yoshida, Y., Olson, J. R., Sillman, S., Martin, R. V., Lamsal, L., Hu, Y., Pickering, K. E., Retscher, C., Allen, D. J., and Crawford, J. H.: Application of OMI observations to a space-based indicator of NO_x and VOC controls

on surface ozone formation, Atmos. Environ., 44, 2213–2223, doi:10.1016/j.atmosenv.2010.03.010, 2010.

Dunlea, E. J., Herndon, S. C., Nelson, D. D., Volkamer, R. M., San Martini, F., Sheehy, P. M., Zahniser, M. S., Shorter, J. H., Wormhoudt, J. C., Lamb, B. K., Allwine, E. J., Gaffney, J. S., Marley, N. A., Grutter, M., Marquez, C., Blanco, S., Cardenas, B., Retama, A., Ramos Villegas, C. R., Kolb, C. E., Molina, L. T., and Molina, M. J.: Evaluation of nitrogen dioxide chemilumines-cence monitors in a polluted urban environment, Atmos. Chem. Phys., 7, 2691–2704, doi:10.5194/acp-7-2691-2007, 2007.

Dubovik, O., Holben, B., Eck, T. F., Smirnov, A., Kaufman, Y. F., King, M. D., Tanré, D., and Slutsker, I.: Variability of absorption and optical properties of key aerosol types observed in world-wide locations, J. Atmos. Sci., 59, 590–608, doi:10.1175/1520-0469(2002)059<0590:VOAAOP>2.0.CO;2, 2002.

Emeis, S. and Schäfer, K.: Remote Sensing Methods to Investigate Boundary-layer Structures relevant to Air Pollution in Cities, Bound.-Lay. Meteorol., 121, 377–385, doi:10.1007/s10546-006-9068-2, 2006.

Fayt, C. and Van Roozendael, M.: WinDOAS 2.1, Software User Manual, available at: http://uv-vis.aeronomie.be/software/WinDOAS/WinDOAS-SUM-210b.pdf (last access: 27 May 2015), Belgian Institute for Space Aeronomy, Brussels, Belgium, 2001.

Finlayson-Pitts, B. J. and Pitts Jr., J. N.: Chemistry of the Upper and Lower Atmosphere, Academic Press, San Diego, CA, 882–886, 2000.

Fioletov, V. E; McLinden, C. A., Krotkov, N., Yang, K., Loyola, D. G., Valks, P., Theys, N., Van Roozendael, M., Nowlan, C. R., Chance, K., Liu, X., Lee, C., and Martin, R. V.: Application of OMI, SCIAMACHY, and GOME-2 satellite SO_2 retrievals for detection of large emission sources, J. Geophys. Res. Atmos. 118, 11399–11418, doi:10.1002/jgrd.50826, 2013.

Fleischmann, O. C., Hartmann, M., Burrows, J. P., and Orphal, J.: New ultraviolet absorption cross-sections of BrO at atmospheric temperatures measured by time-windowing Fourier transform spectroscopy, J. Photochem. Photobiol. A, 168, 117–132, 2004.

Frieß, U., Monks, P. S., Remedios, J. J., Rozanov, A., Sinreich, R., Wagner, T., and Platt, U.: MAX-DOAS O_4 measurements: A new technique to derive information on atmospheric aerosols: 2. Modeling studies, J. Geophys. Res.-Atmos., 111, D14203, doi:10.1029/2005JD006618, 2006.

General, S., Pöhler, D., Sihler, H., Bobrowski, N., Frieß, U., Ziel-cke, J., Horbanski, M., Shepson, P. B., Stirm, B. H., Simpson, W. R., Weber, K., Fischer, C., and Platt, U.: The Heidelberg Airborne Imaging DOAS Instrument (HAIDI) – a novel imag-ing DOAS device for 2-D and 3-D imaging of trace gases and aerosols, Atmos. Meas. Tech., 7, 3459–3485, doi:10.5194/amt-7-3459-2014, 2014.

Gisi, M., Hase, F., Dohe, S., and Blumenstock, T.: Camtracker: a new camera controlled high precision solar tracker sys-tem for FTIR-spectrometers, Atmos. Meas. Tech., 4, 47–54, doi:10.5194/amt-4-47-2011, 2011.

Grainger, J. F. and Ring, J.: Anomalous Fraunhofer line profiles, Nature, 193, 762, doi:10.1038/193762a0, 1962.

Harder, J. W., Williams, E. J., Baumann, K., and Fehsenfeld, F. C.: Ground-based comparison of NO_2, H_2O, and O_3 measured by long-path and in situ techniques during the 1993 Tropospheric

OH Photochemistry Experiment, J. Geophys. Res.-Atmos., 102, 6227–6243, doi:10.1029/96JD01729, 1997.

Heckel, A., Richter, A., Tarsu, T., Wittrock, F., Hak, C., Pundt, I., Junkermann, W., and Burrows, J. P.: MAX-DOAS measurements of formaldehyde in the Po-Valley, Atmos. Chem. Phys., 5, 909–918, doi:10.5194/acp-5-909-2005, 2005.

Hendrick, F., Müller, J.-F., Clémer, K., Wang, P., De Mazière, M., Fayt, C., Gielen, C., Hermans, C., Ma, J. Z., Pinardi, G., Stavrakou, T., Vlemmix, T., and Van Roozendael, M.: Four years of ground-based MAX-DOAS observations of HONO and NO2 in the Beijing area, Atmos. Chem. Phys., 14, 765–781, doi:10.5194/acp-14-765-2014, 2014.

Herman, J., Cede, A., Spinei, E., Mount, G., Tzortziou, M., and Abuhassan, N.: NO_2 column amounts from ground-based Pan-dora and MFDOAS spectrometers using the direct-sun DOAS technique: Intercomparisons and application to OMI validation, J. Geophys. Res., 114, D13307, doi:10.1029/2009JD011848, 2009.

Heue, K.-P., Wagner, T., Broccardo, S. P., Walter, D., Piketh, S. J., Ross, K. E., Beirle, S., and Platt, U.: Direct observation of two dimensional trace gas distributions with an airborne Imag-ing DOAS instrument, Atmos. Chem. Phys., 8, 6707–6717, doi:10.5194/acp-8-6707-2008, 2008.

Hönninger, G., von Friedeburg, C., and Platt, U.: Multi axis dif-ferential optical absorption spectroscopy (MAX-DOAS), Atmos. Chem. Phys., 4, 231–254, doi:10.5194/acp-4-231-2004, 2004.

Irie, H., Takashima, H., Kanaya, Y., Boersma, K. F., Gast, L., Wit-trock, F., Brunner, D., Zhou, Y., and Van Roozendael, M.: Eight-component retrievals from ground-based MAX-DOAS observa-tions, Atmos. Meas. Tech., 4, 1027–1044, doi:10.5194/amt-4-1027-2011, 2011.

Jiménez, R., Martilli, A., Balin, I., v. d. Bergh, H., Calpini, B., Larsen, B. R., Favaro, G., and Kita, D.: Measurement of Formaldehyde (HCHO) by DOAS: Intercomparison to DNPH Measurements and Interpretation from Eulerian Model Calcula-tions, Proceedings of the 93rd Annual Conference & Exhibition, Air & Waste Management Association, Paper #829, Salt Lake City, Utah, 18–22 June 2000.

Jimenez, J. L., Canagaratna, M. R., Donahue, N. M., Prévôt, A. S. H., Zhang, Q., Kroll, J. H., DeCarlo, P. F., Allan, J. D., Coe, H., Ng, N. L., Aiken, A. C., Docherty, K. S., Ulbrich, I. M., Grieshop, A. P., Robinson, A. L., Duplissy, J., Smith, J. D., Wil-son, K. R., Lanz, V. A., Hueglin, C., Sun, Y. L., Tian, J., Laak-sonen, A., Raatikainen, T., Rautiainen, J., Vaattovaara, P., Ehn, M., Kulmala, M., Tomlinson, J. M., Collins, D. R., Cubison, M. J., Dunlea, E. J., Huffman, J. A., Onasch, T. B., Alfarra, M. R., Williams, P. I., Bower, K., Kondo, Y., Schneider, J., Drewnick, F., Borrmann, S., Weimer, S., Demerjian, K., Salcedo, D., Cot-trell, L., Griffin, R., Takami, A., Miyoshi, T., Hatakeyama, S., Shimono, A., Sun, J. Y., Zhang, Y. M., Dzepina, K., Kimmel, J. R., Sueper, D., Jayne, J. T., Herndon, S. C., Trimborn, A. M., Williams, L. R., Wood, E. C., Middlebrook, A. M., Kolb, C. E., Baltensperger, U., and Worsnop, D. R.: Evolution of or-ganic aerosols in the atmosphere, Science, 326, 5959, 1525–1529, doi:10.1126/science.1180353, 2009.

Kanaya, Y., Irie, H., Takashima, H., Iwabuchi, H., Akimoto, H., Sudo, K., Gu, M., Chong, J., Kim, Y. J., Lee, H., Li, A., Si, F., Xu, J., Xie, P.-H., Liu, W.-Q., Dzhola, A., Postylyakov, O., Ivanov, V., Grechko, E., Terpugova, S., and Panchenko, M.: Long-term

MAX-DOAS network observations of NO2 in Russia and Asia (MADRAS) during 2007–2012: instrumentation, elucidation of climatology, and comparisons with OMI satellite observations and global model simulations, Atmos. Chem. Phys. Discuss., 14, 2883–2934, doi:10.5194/acpd-14-2883-2014, 2014.

Kim, K.-H. and Kim, M.-Y.: Comparison of an open path differential optical absorption spectroscopy system and a conventional in situ monitoring system on the basis of long-term measurements of SO_2, NO_2, and O_3, Atmos. Environ., 35, 4059–4072, doi:10.1016/S1352-2310(01)00216-3, 2001.

Kowalewski, M. G. and Janz, S. J.: Remote sensing capabilities of the Airborne Compact Atmospheric Mapper, Proc. SPIE 7452, Earth Observing Systems XIV, 74520Q, 21 August 2009, doi:10.1117/12.827035, 2009.

Li, X., Brauers, T., Shao, M., Garland, R. M., Wagner, T., Deutschmann, T., and Wahner, A.: MAX-DOAS measurements in southern China: retrieval of aerosol extinctions and validation using ground-based in-situ data, Atmos. Chem. Phys., 10, 2079–2089, doi:10.5194/acp-10-2079-2010, 2010.

Lohberger, F., Hönninger, G., and Platt, U.: Ground-based imaging differential optical absorption spectroscopy of atmospheric gases, Appl. Opt. 43, 4711–4717, 2004.

Ma, J. Z., Beirle, S., Jin, J. L., Shaiganfar, R., Yan, P., and Wagner, T.: Tropospheric NO_2 vertical column densities over Beijing: results of the first three years of ground-based MAX-DOAS measurements (2008–2011) and satellite validation, Atmos. Chem. Phys., 13, 1547–1567, doi:10.5194/acp-13-1547-2013, 2013.

Meller, R. and Moortgat, G. K.: Temperature dependence of the absorption cross sections of formaldehyde between 223 and 323 K in the wavelength range 225–375 nm, J. Geophys. Res., 105, 7089–7102, doi:10.1029/1999JD901074, 2000.

Merlaud, A., Van Roozendael, M., Theys, N., Fayt, C., Hermans, C., Quennehen, B., Schwarzenboeck, A., Ancellet, G., Pommier, M., Pelon, J., Burkhart, J., Stohl, A., and De Mazière, M.: Airborne DOAS measurements in Arctic: vertical distributions of aerosol extinction coefficient and NO_2 concentration, Atmos. Chem. Phys., 11, 9219–9236, doi:10.5194/acp-11-9219-2011, 2011.

Oetjen, H., Baidar, S., Krotkov, N. A., Lamsal, L. N., Lechner, M., and Volkamer, R.: Airborne MAX-DOAS measurements over California: Testing the NASA OMI tropospheric NO_2 product, J. Geophys. Res. Atmos., 118, 7400–7413, doi:10.1002/jgrd.50550, 2013.

Ortega, I., Wagner, T., Lampel, J., Van Roozendael, M., Richter, A., Sinha, V., Xie, P., Volkamer, R., and the Glyoxal MAD-CAT Team: Inter-comparison of glyoxal retrievals from MAX-DOAS during the MAD-CAT campaign: EGU General Assembly Conference Abstracts, 15 April 2015, Vol. 17, EGU2015-8194-3, 2015a.

Ortega, I., Coburn, S., Hostetler, C., Ferrare, R., Hair, J., Kassianov, E., Barnard, J., Berg, L., Hodges, G., Lantz, K, and Volkamer, R: The CU 2-D-MAX-DOAS instrument – Part 2: Retrieval of aerosol optical and microphysical properties, to be submitted to Atmos. Meas. Tech. Discuss. 2015b.

Pinardi, G., Van Roozendael, M., Abuhassan, N., Adams, C., Cede, A., Clémer, K., Fayt, C., Frieß, U., Gil, M., Herman, J., Hermans, C., Hendrick, F., Irie, H., Merlaud, A., Navarro Comas, M., Peters, E., Piters, A. J. M., Puentedura, O., Richter, A., Schönhardt, A., Shaiganfar, R., Spinei, E., Strong, K., Takashima, H., Vrekoussis, M., Wagner, T., Wittrock, F., and Yilmaz, S.: MAX-DOAS formaldehyde slant column measurements during CINDI: intercomparison and analysis improvement, Atmos. Meas. Tech., 6, 167–185, doi:10.5194/amt-6-167-2013, 2013.

Piters, A. J. M., Boersma, K. F., Kroon, M., Hains, J. C., Van Roozendael, M., Wittrock, F., Abuhassan, N., Adams, C., Akrami, M., Allaart, M. A. F., Apituley, A., Beirle, S., Bergwerff, J. B., Berkhout, A. J. C., Brunner, D., Cede, A., Chong, J., Clémer, K., Fayt, C., Frieß, U., Gast, L. F. L., Gil-Ojeda, M., Goutail, F., Graves, R., Griesfeller, A., Großmann, K., Hemerijckx, G., Hendrick, F., Henzing, B., Herman, J., Hermans, C., Hoexum, M., van der Hoff, G. R., Irie, H., Johnston, P. V., Kanaya, Y., Kim, Y. J., Klein Baltink, H., Kreher, K., de Leeuw, G., Leigh, R., Merlaud, A., Moerman, M. M., Monks, P. S., Mount, G. H., Navarro-Comas, M., Oetjen, H., Pazmino, A., Perez-Camacho, M., Peters, E., du Piesanie, A., Pinardi, G., Puentedura, O., Richter, A., Roscoe, H. K., Schönhardt, A., Schwarzenbach, B., Shaiganfar, R., Sluis, W., Spinei, E., Stolk, A. P., Strong, K., Swart, D. P. J., Takashima, H., Vlemmix, T., Vrekoussis, M., Wagner, T., Whyte, C., Wilson, K. M., Yela, M., Yilmaz, S., Zieger, P., and Zhou, Y.: The Cabauw Intercomparison campaign for Nitrogen Dioxide measuring Instruments (CINDI): design, execution, and early results, Atmos. Meas. Tech., 5, 457–485, doi:10.5194/amt-5-457-2012, 2012.

Platt, U. and Stutz, J.: Differential Optical Absorption Spectroscopy, 597 pp., Springer, Berlin, doi:10.1007/978-3-540-75776-4, 2008.

Prados-Roman, C., Butz, A., Deutschmann, T., Dorf, M., Kritten, L., Minikin, A., Platt, U., Schlager, H., Sihler, H., Theys, N., Van Roozendael, M., Wagner, T., and Pfeilsticker, K.: Airborne DOAS limb measurements of tropospheric trace gas profiles: case studies on the profile retrieval of O4 and BrO, Atmos. Meas. Tech., 4, 1241–1260, doi:10.5194/amt-4-1241-2011, 2011.

Remmers, J., Wagner, T., and the MADCAT team.: Azimuthal variability of trace gases and aerosols measured during the MAD-CAT campaign in summer 2013 in Mainz, Germany: EGU General Assembly Conference Abstracts, Vol. 17, EGU2015-5018, 15 April 2015.

Rodgers, C. D.: Characterization and error analysis of profiles retrieved from remote sounding measurements, J. Geophys. Res.-Atmos., 95, 5587–5595, doi:10.1029/JD095iD05p05587, 1990.

Rodgers, C. D.: Inverse Methods for Atmospheric Sounding: Theory and Practice, vol. 2, World Scientific, Singapore, 256 pp., 2000.

Roscoe, H. K., Van Roozendael, M., Fayt, C., du Piesanie, A., Abuhassan, N., Adams, C., Akrami, M., Cede, A., Chong, J., Clémer, K., Friess, U., Gil Ojeda, M., Goutail, F., Graves, R., Griesfeller, A., Grossmann, K., Hemerijckx, G., Hendrick, F., Herman, J., Hermans, C., Irie, H., Johnston, P. V., Kanaya, Y., Kreher, K., Leigh, R., Merlaud, A., Mount, G. H., Navarro, M., Oetjen, H., Pazmino, A., Perez-Camacho, M., Peters, E., Pinardi, G., Puentedura, O., Richter, A., Schönhardt, A., Shaiganfar, R., Spinei, E., Strong, K., Takashima, H., Vlemmix, T., Vrekoussis, M., Wagner, T., Wittrock, F., Yela, M., Yilmaz, S., Boersma, F., Hains, J., Kroon, M., Piters, A., and Kim, Y. J.: Intercomparison of slant column measurements of NO_2 and O_4 by MAX-DOAS and zenith-sky UV and visible spectrometers, Atmos. Meas. Tech., 3, 1629–1646, doi:10.5194/amt-3-1629-2010, 2010.

Rothman, L. S., Gordon, I. E., Barber, R. J., Dothe, H., Gamache, R. R., Goldman, A., Perevalov, V. I., Tashkun, S. A., and

Tennyson, J.: HITEMP, the high-temperature molecular spectroscopic database, J. Quant. Spectrosc. Ra, 111, 2139–2150, doi:10.1016/j.jqsrt.2010.05.001, 2010.

Ryerson, T. B., Andrews, A. E., Angevine, W. M., Bates, T. S., Brock, C. A., Cohen, R. C., Cooper, O. R., de Gouw, J. A., Fehsenfeld, F. C., Ferrare, R. A., Fischer, M. L., Flagan, R. C., Goldstein, A. H., Hair, J. W., Hardesty, R. M., Hostetler, C. A., Jimenez, J. L., Langford, A. O., McCauley, E., McKeen, S. A., Molina, L. T., Nenes, A., Oltmans, S. J., Parrish, D. D., Pederson, J. R., Pierce, R. B., Prather, K., Quinn, P. K., Seinfeld, J. H., Senff, C., Sorooshian, A., Stutz, J., Surratt, J. D., Trainer, M., Volkmer, R., Williams, E. J., and Wofsy, S. C.: The 2010 California Research at the Nexus of Air Quality and Climate Change (CalNex) field study, J. Geophys. Res.-Atmos., 118, 5830–5866, doi:10.1002/jgrd.50331, 2013.

Schofield, R., Connor, B. J., Kreher, K., Johnston, P. V., and Rodgers, C. D.: The retrieval of profile and chemical information from ground-based UV-visible spectroscopic measurements, J. Quant. Spectrosc. Ra., 86, 115–131, doi:10.1016/S0022-4073(03)00278-4, 2004.

Shaiganfar, R., Beirle, S., Sharma, M., Chauhan, A., Singh, R. P., and Wagner, T.: Estimation of NO_x emissions from Delhi using Car MAX-DOAS observations and comparison with OMI satellite data, Atmos. Chem. Phys., 11, 10871–10887, doi:10.5194/acp-11-10871-2011, 2011.

Sinreich, R., Frieß, U., Wagner, T., and Platt, U.: Multi axis differential optical absorption spectroscopy (MAX-DOAS) of gas and aerosol distributions, Faraday Discuss., 130, 153–164, doi:10.1039/B419274P, 2005.

Sinreich, R., Coburn, S., Dix, B., and Volkamer, R.: Ship-based detection of glyoxal over the remote tropical Pacific Ocean, Atmos. Chem. Phys., 10, 11359–11371, doi:10.5194/acp-10-11359-2010, 2010.

Sinreich, R., Merten, A., Molina, L., and Volkamer, R.: Parameterizing radiative transfer to convert MAX-DOAS dSCDs into near-surface box-averaged mixing ratios, Atmos. Meas. Tech., 6, 1521–1532, doi:10.5194/amt-6-1521-2013, 2013.

Spinei, E., Cede, A., Herman, J., Mount, G. H., Eloranta, E., Morley, B., Baidar, S., Dix, B., Ortega, I., Koenig, T., and Volkamer, R.: Ground-based direct-sun DOAS and airborne MAX-DOAS measurements of the collision-induced oxygen complex, O_2O_2, absorption with significant pressure and temperature differences, Atmos. Meas. Tech., 8, 793–809, doi:10.5194/amt-8-793-2015, 2015.

Steck, T.: Methods for determining regularization for atmospheric retrieval problems, Appl. Optics, 41, 973, 1788–1797, doi:10.1364/AO.41.001788, 2002.

Thalman, R. and Volkamer, R.: Temperature dependent absorption cross-sections of O_2-O_2 collision pairs between 340 and 630 nm and at atmospherically relevant pressure, Phys. Chem. Chem. Phys., 15, 15371–15381, doi:10.1039/c3cp50968k, 2013.

Thalman, R., Baeza-Romero, M. T., Ball, S. M., Borrás, E., Daniels, M. J. S., Goodall, I. C. A., Henry, S. B., Karl, T., Keutsch, F. N., Kim, S., Mak, J., Monks, P. S., Muñoz, A., Orlando, J., Peppe, S., Rickard, A. R., Ródenas, M., Sánchez, P., Seco, R., Su, L., Tyndall, G., Vázquez, M., Vera, T., Waxman, E., and Volkamer, R.: Instrument intercomparison of glyoxal, methyl glyoxal and NO_2 under simulated atmospheric conditions, Atmos. Meas. Tech., 8, 1835–1862, doi:10.5194/amt-8-1835-2015, 2015.

Thornton, J. A., Wooldridge, P. J., Cohen, R. C., Williams, E. J., Hereid, D., Fehsenfeld, F. C., Stutz, J., and Alicke, B.: Comparisons of in situ and long path measurements of NO_2 in urban plumes, J. Geophys. Res., 108, 4496, doi:10.1029/2003JD003559, 2003.

Vandaele, A. C., Hermans, C., Simon, P. C., Carleer, M., Colin, R., Fally, S., M'erienne, M. F., Jenouvrier, A., and Coquart, B.: Measurements of the NO_2 absorption cross-section from $42\,000\,cm^{-1}$ to $10\,000\,cm^{-1}$ (238–1000 nm) at 220 K and 294 K., J. Quant. Spectrosc. Ra., 59, 171–184, doi:10.1016/S0022-4073(97)00168-4, 1998.

Villena, G., Bejan, I., Kurtenbach, R., Wiesen, P., and Kleffmann, J.: Interferences of commercial NO_2 instruments in the urban atmosphere and in a smog chamber, Atmos. Meas. Tech., 5, 149–159, doi:10.5194/amt-5-149-2012, 2012.

Vlemmix, T., Piters, A. J. M., Berkhout, A. J. C., Gast, L. F. L., Wang, P., and Levelt, P. F.: Ability of the MAX-DOAS method to derive profile information for NO_2: can the boundary layer and free troposphere be separated?, Atmos. Meas. Tech., 4, 2659–2684, doi:10.5194/amt-4-2659-2011, 2011.

Volkamer, R., Spietz, P., Burrows, J., and Platt, U.: High resolution absorption cross-section of glyoxal in the UV-vis and IR spectral ranges, J. Photoch. Photobio. A, 172, 35–46, doi:10.1016/j.jphotochem.2004.11.011, 2005.

Volkamer, R., San Martini, F., Molina, L. T., Salcedo, D., Jimenez, J. L., and Molina, M. J.: A missing sink for gas-phase glyoxal in Mexico City: Formation of secondary organic aerosol, Geophys. Res. Lett., 34, L19807, doi:10.1029/2007GL030752, 2007.

Volkamer, R., Baidar, S., Campos, T. L., Coburn, S., DiGangi, J. P., Dix, B., Eloranta, E. W., Koenig, T. K., Morley, B., Ortega, I., Pierce, B. R., Reeves, M., Sinreich, R., Wang, S., Zondlo, M. A., and Romashkin, P. A.: Aircraft measurements of BrO, IO, glyoxal, NO_2, H_2O, O_2–O_2 and aerosol extinction profiles in the tropics: comparison with aircraft-/ship-based in situ and lidar measurements, Atmos. Meas. Tech., 8, 2121–2148, doi:10.5194/amt-8-2121-2015, 2015.

Volten, H., Brinksma, E. J., Berkhout, A. J. C., Hains, J., Bergwerff, J. B., Van der Hoff, G. R., Apituley, A., Dirksen, R. J., Calabretta-Jongen, S., and Swart, D. P. J.: NO_2 Lidar Profile Measurements for Satellite Interpretation and Validation, J. Geophys. Res.-Atmos., 114, D24301, doi:10.1029/2009JD012441, 2009.

Vrekoussis, M., Wittrock, F., Richter, A., and Burrows, J. P.: GOME-2 observations of oxygenated VOCs: what can we learn from the ratio glyoxal to formaldehyde on a global scale?, Atmos. Chem. Phys., 10, 10145–10160, doi:10.5194/acp-10-10145-2010, 2010.

Wagner, T., Burrows, J. P., Deutschmann, T., Dix, B., von Friedeburg, C., Frieß, U., Hendrick, F., Heue, K.-P., Irie, H., Iwabuchi, H., Kanaya, Y., Keller, J., McLinden, C. A., Oetjen, H., Palazzi, E., Petritoli, A., Platt, U., Postylyakov, O., Pukite, J., Richter, A., van Roozendael, M., Rozanov, A., Rozanov, V., Sinreich, R., Sanghavi, S., and Wittrock, F.: Comparison of box-air-mass-factors and radiances for Multiple-Axis Differential Optical Absorption Spectroscopy (MAX-DOAS) geometries calculated from different UV/visible radiative transfer models, Atmos. Chem. Phys., 7, 1809–1833, doi:10.5194/acp-7-1809-2007, 2007.

Wagner, T., Beirle, S., and Deutschmann, T.: Three-dimensional simulation of the Ring effect in observations of scattered sun light using Monte Carlo radiative transfer models, Atmos. Meas. Tech., 2, 113–124, doi:10.5194/amt-2-113-2009, 2009.

Wagner, T., Beirle, S., Brauers, T., Deutschmann, T., Frieß, U., Hak, C., Halla, J. D., Heue, K. P., Junkermann, W., Li, X., Platt, U., and Pundt-Gruber, I.: Inversion of tropospheric profiles of aerosol extinction and HCHO and NO_2 mixing ratios from MAX-DOAS observations in Milano during the summer of 2003 and comparison with independent data sets, Atmos. Meas. Tech., 4, 2685–2715, doi:10.5194/amt-4-2685-2011, 2011.

Wang, Y., Li, A., Xie, P. H., Wagner, T., Chen, H., Liu, W. Q., and Liu, J. G.: A rapid method to derive horizontal distributions of trace gases and aerosols near the surface using multi-axis differential optical absorption spectroscopy, Atmos. Meas. Tech., 7, 1663–1680, doi:10.5194/amt-7-1663-2014, 2014.

Wang, Y., Wagner, T., Xie, P., Remmers, J., Li, A., Lampell, J., Friess, Udo., Peters, E., Wittrock, F., Richter A., Hilboll, A., Volkamer, R., Ortega, I., Hendrick, F., Van Roozendael, M., Ma, J., Su, H., and Cheng, Y.: Intercomparison of HONO SCDs and profiles from MAX-DOAS observations during the MAD-CAT campaign and comparison to chemical model simulations: EGU General Assembly Conference Abstracts, 15 April 2015, Vol. 17, EGU2015-4674-1, 2015.

Wittrock, F., Oetjen, H., Richter, A., Fietkau, S., Medeke, T., Rozanov, A., and Burrows, J. P.: MAX-DOAS measurements of atmospheric trace gases in Ny-Ålesund - Radiative transfer studies and their application, Atmos. Chem. Phys., 4, 955–966, doi:10.5194/acp-4-955-2004, 2004.

Zhang, Q., Jimenez, J. L., Canagaratna, M. R., Allan, J. D., Coe, H., Ulbrich, I., Alfarra, M. R., Takami, A., Middlebrook, A. M., Sun, Y. L., Dzepina, K., Dunlea, E., Docherty, K., De-Carlo, P. F., Salcedo, D., Onasch, T., Jayne, J. T., Miyoshi, T., Shimono, A., Hatakeyama, S., Takegawa, N., Kondo, Y., Schneider, J., Drewnick, F., Borrmann, S., Weimer, S., Demer-jian, K., Williams, P., Bower, K., Bahreini, R., Cottrell, L., Griffin, R. J., Rautiainen, J., Sun, J. Y., Zhang, Y. M., and Worsnop, D. R.: Ubiquity and dominance of oxygenated species in organic aerosols in anthropogenically-influenced Northern Hemisphere midlatitudes, Geophys. Res. Lett., 34, L13801, doi:10.1029/2007GL029979, 2007.